

1
2
3
4
5
6
7
8
9
10
11
12
13
14
15
16
17
18
19
20
21
22
23
24
25
26
27

GTS v1.0: A Macrophysics Scheme for Climate Models Based on a Probability
Density Function

Chein-Jung Shiu^{1,*}, Yi-Chi Wang¹, Huang-Hsiung Hsu¹, Wei-Ting Chen², Hua-Lu
Pan³, Ruiyu Sun⁴, Yi-Hsuan Chen⁵, and Cheng-An Chen¹

- 1 Research Center for Environmental Changes, Academia Sinica, Taiwan
- 2 Department of Atmospheric Sciences, National Taiwan University, Taiwan
- 3 Retired Senior Scientist, National Centers for Environmental Prediction, NOAA,
USA
- 4 National Centers for Environmental Prediction, NOAA, USA
- 5 Department of Climate and Space Sciences and Engineering, University of
Michigan, USA

Correspondence: Chein-Jung Shiu (email: cjshiu@rcec.sinica.edu.tw)

28

29 Short title: Macrophysics for Climate Models

30

31 Key points:

32 1) A cloud macrophysics scheme utilizing grid-mean hydrometeor information is
33 developed and evaluated for climate models.

34 2) The GFS-TaiESM-Sundqvist (GTS) scheme can simulate variations of cloud fraction
35 associated with relative humidity (RH) in a more consistent way than the default
36 scheme of CAM5.3.

37 3) Through better cloud–RH distributions, the GTS scheme helps to better represent
38 cloud fraction, cloud radiative forcing, and thermodynamic-related climatic fields in
39 climate simulations.

40

41

42

43 Abstract

44 Cloud macrophysics schemes are unique parameterizations for general circulation
45 models. We propose an approach based on a probability density function (PDF) that
46 utilizes cloud condensates and saturation ratios to replace the assumption of critical
47 relative humidity (RH). We test this approach, called the GFS-TaiESM-Sundqvist (GTS)
48 scheme, using the macrophysics scheme within the Community Atmospheric Model
49 version 5.3 (CAM5.3) framework. Via single-column model results, the new approach
50 simulates the cloud fraction (CF)–RH distributions closer to those of the observations
51 when compared to those of the default CAM5.3 scheme. We also validate the impact of
52 the GTS scheme on global climate simulations with satellite observations. The
53 simulated CF is comparable to CloudSat/CALIPSO data. Comparisons of the vertical
54 distributions of CF and cloud water content (CWC), as functions of large-scale dynamic
55 and thermodynamic parameters, with the CloudSat/CALIPSO data suggest that the
56 GTS scheme can closely simulate observations. This is particularly noticeable for
57 thermodynamic parameters, such as RH, upper-tropospheric temperature, and total
58 precipitable water, implying that our scheme can simulate variation in CF associated
59 with RH more reliably than the default scheme. Changes in CF and CWC would affect
60 climatic fields and large-scale circulation via cloud–radiation interactions. Both
61 climatological means and annual cycles of many of the GTS-simulated variables are
62 improved compared with the default scheme, particularly with respect to water vapor
63 and RH fields. Different PDF shapes in the GTS scheme also significantly affect global
64 simulations.

65

66

67

68 1. Introduction

69

70 Global weather and climate models commonly use cloud macrophysics
71 parameterization to calculate the sub-grid cloud fraction (CF) and/or large-scale cloud
72 condensate, as well as cloud overlap, which is required in cloud microphysics and
73 radiation schemes [Slingo, 1987; Sundqvist, 1988; Sundqvist *et al.*, 1989; Smith, 1990;
74 Tiedtke, 1993; Xu and Randall, 1996; Rasch and Kristjansson, 1998; Jakob and Klein,
75 2000; Tompkins, 2002; Zhang *et al.*, 2003; Wilson *et al.*, 2008a,b; Chabourea and
76 Bechtold, 2012; Park *et al.*, 2014; Park *et al.*, 2016]. The largest uncertainty in climate
77 prediction is associated with clouds and aerosols [Boucher *et al.*, 2013]. The large
78 number of cloud-related parameterizations in general circulation models (GCM)
79 contributes to this uncertainty. In recent years, an increasing amount of research has
80 been devoted to unifying cloud-related parameterizations, for example by incorporating
81 the planetary boundary layer, shallow and/or deep convections, and stratiform cloud
82 (cloud macrophysics and/or microphysics) parameterizations, to improve cloud
83 simulations in large-scale global models [Bogenschutz *et al.*, 2013; Park *et al.*, 2014a,
84 2014b; Storer *et al.*, 2015].

85 Some of these parameterizations use prognostic approaches to parameterize the CF
86 [Tiedtke, 1993; Tompkins, 2002; Wilson *et al.*, 2008a, b; Park *et al.*, 2016] while others
87 use diagnostic approaches [Sundqvist *et al.*, 1989; Smith, 1990; Xu and Randall, 1996;
88 Zhang *et al.*, 2003; Park *et al.*, 2014]. Most of the diagnostic approaches used in GCM
89 cloud macrophysical schemes use the critical relative humidity threshold (RH_c) to
90 calculate CF [Slingo, 1987; Sundqvist *et al.*, 1989; Roeckner *et al.*, 1996]. In this type
91 of parameterization, GCMs frequently use the RH_c value as a tunable parameter
92 [Mauritsen *et al.*, 2012; Golaz *et al.*, 2013; Hourdin *et al.*, 2016]. There are some studies
93 on the verification of global simulations focused on the cloud macrophysical
94 parameterization [Hogan *et al.*, 2009; Franklin *et al.*, 2012; Qian *et al.*, 2012;
95 Sotiropoulou *et al.*, 2015]. In addition, many model development studies show the
96 impact of total water used in CF schemes on global simulations after modifying the RH_c
97 and/or the probability density function (PDF) [Donner *et al.*, 2011; Neale *et al.*, 2013;
98 Schmidt *et al.*, 2014]. Some recent studies have attempted to constrain RH_c from
99 regional sounding observations and/or satellite retrievals to improve regional and/or
100 global simulations [Quaas, 2012; Molod, 2012; Lin, 2014].

101 While many variations of the diagnostic Sundqvist CF scheme have been proposed,
102 most numerical weather prediction models and GCMs use the basic principle proposed
103 by Sundqvist *et al.* [1989]: the changes in cloud condensate in a grid box are derived
104 from the budget equation for RH. In the meantime, the amount of additional moisture
105 from other processes is divided between the cloudy portion and the clear portion

106 according to the proportion of clouds determined using an assumed RH_c . While changes
107 have been made to other parts of the Sundqvist scheme, the $CF-RH_c$ relationship still
108 applies in most Sundqvist-based schemes. As highlighted by Thompkins [2005], the
109 RH_c value in the Sundqvist scheme can be related to the assumption of uniform
110 distribution for the total water in an unsaturated grid box such that the distribution width
111 (δ_c) of the situation when a cloud is about to form is given by:

$$112 \quad \delta_c = q_s(1 - RH_c), \quad (1)$$

113 where q_s is the saturated mixing ratio.

114 We re-derived this equation by describing the change in the distribution width δ with
115 grid-mean cloud condensates and saturation ratio using the basic assumption of uniform
116 distribution from Sundqvist *et al.* [1989] rather than using the RH_c -derived δ_c , thereby
117 eliminating unnecessary use of the RH_c while retaining the PDF assumption for the
118 entire scheme. This modified macrophysics scheme is named the GFS-TaiESM-
119 Sundqvist (GTS) scheme version 1.0 (GTS v1.0). It was first developed for the Global
120 Forecast System (GFS) model at the National Centers for Environmental Protection
121 (NCEP) and has been further improved for the Taiwan Earth System Model (TaiESM;
122 Lee *et al.*, 2020) at the Research Center for Environmental Changes (RCEC), Academia
123 Sinica. Park *et al.* [2014] discussed a similar approach wherein a triangular PDF was
124 used to diagnose cloud liquid water as well as the cloud liquid fraction, and suggested
125 that the PDF width could be computed internally rather than specified, to consistently
126 diagnose both CF and cloud liquid water as in macrophysics. These authors also
127 mentioned that such stratus cloud macrophysics could be applied across any horizontal
128 and vertical resolution of a GCM grid, although they did not formally implement and
129 test this idea using their scheme. Building upon their ideas, we implemented and tested
130 this assumption with a triangular PDF in the GTS scheme.

131 In summary, this GTS scheme adopts Sundqvist's assumption regarding the partition
132 of cloudy and clear regions within a model grid box but uses a variable PDF width once
133 clouds are formed. It introduces a self-consistent diagnostic calculation of CF. Owing
134 to their use of an internally computed PDF width, GTS schemes are expected to be able
135 to better represent the relative variation of CF with RH in GCM grids.

136 A variety of assumptions regarding PDF shape can be adopted in diagnostic
137 approaches [Sommeria and Deardorff, 1977; Bougeault, 1982; Smith, 1990; Tompkins,
138 2002]. Some studies have investigated representing cloud condensate and water vapor
139 in a more statistically accurate way by using more complex types of PDF to represent
140 parameters such as total water, CF, and updraft vertical velocity [Larson, 2002; Golaz
141 *et al.*, 2002; Firl, 2013; Bogenschutz *et al.*, 2012; Bogenschutz and Krueger, 2013; Firl
142 and Randall, 2015]. In this study, we apply and investigate two simple and commonly
143 used PDF shapes—uniform and triangular—in our parameterization of the GTS

144 macrophysics scheme. Other complex types of PDF assumptions can also be used if
145 analytical solutions regarding the width of the PDF can be derived.

146 Most of the studies mentioned above estimate the CF via cloud liquid or total cloud
147 water. Earlier versions of GCMs used a Slingo-type approach to resolve the cloud ice
148 fraction [Slingo, 1987; Tompkins *et al.*, 2007; Park *et al.*, 2014]. On the other hand, the
149 current generation of global models participating in the Coupled Model
150 Intercomparison Project Phase 6 (CMIP6) have alternative approaches for the handling
151 of CFs associated with ice clouds. In the GTS scheme, the approach to cloud liquid-
152 water fraction parameterization is extended to the cloud ice fraction as well, wherein
153 the saturation-mixing ratio (q_s) with respect to water is replaced by q_s with respect to
154 ice. This provides a consistent treatment for the cloud liquid and cloud ice fractions.
155 Many studies have argued that the assumption of rapid adjustment between water vapor
156 and cloud liquid water applied in GCM CF schemes cannot be applied to ice clouds
157 [Tompkins *et al.*, 2007; Salzmman *et al.*, 2010; Chosson *et al.*, 2014]. In addition, it
158 would be difficult to represent the CF of mixed-phase clouds using such an assumption
159 [McCoy *et al.*, 2016]. Applying a diagnostic approach to the cloud ice fraction similar
160 to that used for the cloud liquid fraction is indeed challenging and may result in a high
161 level of uncertainty. To investigate this issue, we also conduct a series of sensitivity
162 tests related to the super-saturation ratio assumption, which is applied when calculating
163 the cloud ice fraction in the GTS scheme.

164

165 2. Descriptions of scheme, model, and simulation setup

166

167 2.1 Scheme descriptions

168 Figure 1 illustrates the PDF-based scheme with a uniform PDF and a triangular PDF
169 of total water substance q_t . By assuming that the clear region is free of condensates and
170 that the cloudy region is fully saturated, the cloudy region (b) becomes the area where
171 q_t is larger than the saturation value q_s (shaded area). The PDF-based scheme
172 automatically retains consistency between CF and condensates because it is derived
173 from the same PDF. Here, we used the uniform PDF to demonstrate the relationship
174 between RH_c and the width of the PDF. Using a derivation extended from Tompkins
175 [2005]:

$$176 \quad b = \frac{1}{2\delta} (\overline{q_t} + \delta - q_s). \quad (2)$$

177 It is evident that, with the uniform PDF:

$$178 \quad \delta_c = q_s(1 - RH_c). \quad (3)$$

179 Therefore, $RH_c = 1 - \frac{\delta_c}{q_s}$. Thus, if the width δ of the uniform PDF is determined, then

180 RH_c can be determined accordingly. This relation reveals that the RH_c assumption of
 181 the RH-based scheme actually assumes the width of the uniform PDF to be δ_c from the
 182 PDF-based scheme. As noticed by Thompkins [2005], the RH_c used by Sundqvist *et al.*
 183 [1989] for cloud generation can be linked to the statistical cloud scheme with a uniform
 184 distribution. Building upon this finding, we eliminated the assumption of RH_c by
 185 determining the $P(q_t)$ with information about \bar{q}_v and \bar{q}_l provided by the base model.
 186 Please note that uniform temperature is assumed over the grid for the GTS scheme.

187 With uniform PDF as denoted in Figure 1 (a), the liquid cloud fraction (b_l) and grid-
 188 mean cloud-liquid mixing ratio (\bar{q}_l) can be integrated as follows:

$$189 \quad b_l = \int_{q_s}^{\infty} P(q_t) dq_t = \frac{1}{2\delta} (\bar{q}_l + \bar{q}_v + \delta - q_s), \quad (4)$$

190 and:

$$191 \quad \bar{q}_l = \int_{q_s}^{\infty} (q_t - q_s) P(q_t) dq_t = \frac{1}{4\delta} (\bar{q}_l + \delta - q_s). \quad (5)$$

192 Given \bar{q}_l , \bar{q}_v , and q_s , the width of uniform PDF can be determined as follows:

$$193 \quad \delta = (\sqrt{\bar{q}_l} + \sqrt{q_s - \bar{q}_v})^2. \quad (6)$$

194 Therefore, we can calculate the liquid cloud fraction from equation (4).

195 In addition to the application of a PDF-based approach for liquid CF
 196 parameterization, the GTS scheme also uses the same concept for parameterizing the
 197 ice CF (b_i) as follows:

$$198 \quad b_i = \frac{1}{2\delta} (\bar{q}_i + \bar{q}_v + \delta - sup * q_{si}), \quad (7)$$

199 where \bar{q}_i , \bar{q}_v , and q_{si} denote the grid-mean cloud-ice mixing ratio, water-vapor mixing
 200 ratio, and saturation mixing ratio over ice, respectively. In equation (7), q_{si} is multiplied
 201 by a supersaturation factor (*sup*) to account for the situation in which rapid saturation
 202 adjustment is not reached for cloud ice. In the present version of the GTS scheme, *sup*
 203 is temporarily assumed to be 1.0. Sensitivity tests regarding *sup* will be discussed in
 204 Section 5.7. Values of \bar{q}_i and \bar{q}_v used to calculate equation (7) are the updated state
 205 variables before calling the cloud macrophysics process.

206 A more complex PDF can be used for $P(q_t)$ instead of the uniform distribution in
 207 our derivation. For example, the Community Atmospheric Model version 5.3 (CAM5.3)
 208 macrophysics model adopts a triangular PDF instead of a uniform PDF to represent the
 209 sub-grid distribution of the total water substance [Park *et al.*, 2014]. Mathematically,
 210 the triangular distribution is a more accurate approximation of the Gaussian distribution
 211 than the uniform distribution and it may also be more realistic. Therefore, we followed
 212 the same procedure to diagnose the CF by forming a triangular PDF with \bar{q}_l , \bar{q}_v , and \bar{q}_s
 213 provided. Moreover, by using a triangular PDF, we can obtain results that are more

214 comparable with the CAM5.3 macrophysics scheme because the same PDF was used.
 215 By considering the PDF width, the CF (b) and liquid water content (\bar{q}_l) can be written
 216 as follows:

$$217 \quad b = \begin{cases} \frac{1}{2}(1 - s_s)^2 & \text{if } s_s > 0 \\ 1 - \frac{1}{2}(1 + s_s)^2 & \text{if } s_s < 0 \end{cases} \quad (8)$$

218 and:

$$219 \quad \frac{\bar{q}_l}{\delta} = \begin{cases} \frac{1}{6} - \frac{s_s^2}{6} + \frac{s_s^3}{6} - s_s b & \text{if } s_s > 0 \\ -\frac{1}{6} - \frac{1}{6}(3s_s^2 - 2s_s^3) - s_s b & \text{if } s_s < 0 \end{cases}, \quad (9)$$

220 respectively, where $s_s = \frac{q_s - \bar{q}_t}{\delta}$. From these two equations, we can derive the width of

221 the triangular PDF and calculate the CF (b) based on q_s , \bar{q}_t , and \bar{q}_v instead of RH_c .
 222 Detailed derivations of equations (8) and (9) can be seen in the Appendix A. Notably,
 223 the PDF width for the total water substance can only be constrained when the cloud
 224 exists. Therefore, the RH_c is still required when clouds start to form from a clear region.
 225 To simplify the cloud macrophysics parameterization, value of RH_c in GTS scheme is
 226 assumed to be 0.8 instead of RH_c varying with height in the default Park scheme. The
 227 GTS scheme still uses the default prognostic scheme for calculating cloud condensates
 228 [Park *et al.*, 2014] and it takes effects only on the stratiform CFs. Although the GTS
 229 scheme is presumed to have good consistency between CF and condensates, the
 230 consistency check subroutines of the Park scheme are still kept in the GTS scheme to
 231 avoid “empty” and “dense” clouds due to the usage of Park scheme for calculating
 232 cloud condensates and the GTS schemes still need RH_c when clouds start to form.

233 In this study, GTS schemes utilizing two different PDF shape assumptions are
 234 evaluated: uniform (hereafter, U_pdf) and triangular (hereafter, T_pdf). These two PDF
 235 types are specifically formulated to evaluate the effects of the choice of PDF shape. A
 236 triangular PDF is the default shape used for cloud macrophysics by the Community
 237 Atmospheric Model version 5.3 (CAM5.3; hereafter, the Park scheme). The T_pdf of
 238 the GTS scheme is numerically similar to that of the Park scheme except for using a
 239 variable width for the triangular PDF once clouds are formed.

240

241 2.2 Model description and simulation setup

242 The GTS schemes described in this study were implemented into CAM5.3 in the
 243 Community Earth System Model version 1.2.2 (CESM 1.2.2), which is developed and
 244 maintained by DOE UCAR/NCAR. Physical parameterizations of CAM5.3 include
 245 deep convection, shallow convection, macrophysics, aerosol activation, stratiform
 246 microphysics, wet deposition of aerosols, radiation, a chemistry and aerosol module,

247 moist turbulence, dry deposition of aerosols, and dynamics. References for the
248 individual physical parameterizations can be found in the NCAR technical notes [Neale
249 *et al.*, 2010]. The master equations are solved on a vertical hybrid pressure–sigma
250 coordinate system (30 vertical levels) using the finite-volume dynamical core option of
251 CAM5.3.

252 We conducted both the single-column tests and stand-alone global-domain
253 simulations with CAM5.3 physics. The single-column setup provides the benefit of
254 understanding the responses of physical schemes under environmental forcing of
255 different regimes of interest. Here, we adopt the case of Tropical Western Pacific–
256 International Cloud Experiment (TWP-ICE), which was supported by the ARM
257 program of the Department of Energy and the Bureau of Meteorology of Australia from
258 January to February 2006 over Darwin in Northern Australia. Based on the
259 meteorological conditions, the TWP-ICE period can be divided into four shorter periods:
260 the active monsoon period (19–25 January), the suppressed monsoon period (26
261 January to 2 February), the monsoon clear-sky period (3–5 February), and the monsoon
262 break period (6–13 February, May *et al.* [2008]; Xie *et al.* [2010]). To take advantage
263 of previous studies of cloud-resolving models and single-column models, we followed
264 the setup of Franklin *et al.* [2012] to initiate the single-column runs starting on 19
265 January, 2006, and running for 25 days.

266 Stand-alone CAM5.3 simulations of the CESM model, forced by climatological sea
267 surface temperature for the year 2000 (*i.e.*, CESM compset: F_2000_CAM5), are
268 conducted to demonstrate global results. The horizontal resolution of the CESM global
269 runs is set at 2°. Individual global simulations are integrated for 12 years, and the output
270 for the last 10 years is used to calculate climatological means and annual cycles in
271 global means. Because we made changes largely with respect to CF, we also conducted
272 corresponding simulations using the satellite-simulator approach to provide CF for a
273 fair comparison with satellite CF products and typical CESM model output. This was
274 done using the CFMIP Observation Simulator Package (COSP) built into CESM 1.2.2
275 [Kay *et al.*, 2012]. In addition to the default monthly outputs, daily outputs of several
276 selected variables are also written out for more in-depth analysis.

277

278

279 3. Observational datasets and offline calculations

280

281 3.1 Observational data

282 Cloud field comparisons are critical for modifications to our system with respect to
283 cloud macrophysical schemes. Therefore, we use the products from
284 CloudSat/CALIPSO to provide CF data for evaluating the modeling capabilities of the

285 default and modified GTS cloud macrophysical schemes. This dataset (provided by the
286 AMWG diagnostics package of NCAR) is used to compare with CF simulated by the
287 COSP satellite simulator of CESM 1.2.2. Notably, this dataset is different from the one
288 below which also includes cloud water content (CWC).

289 In addition to cloud observations, observational radiation fluxes from CERES-EBAF
290 are also used to investigate whether simulations using our system will improve radiation
291 calculations for both shortwave and longwave radiation flux, as well as their
292 corresponding cloud radiative forcings. Precipitation data are compared with Global
293 Precipitation Climatology Project data and several other climatic parameters, *e.g.*, air
294 temperature, RH, precipitable water, and zonal wind, are evaluated against the
295 reanalysis data (ERA-Interim). All these observational data are also obtained from the
296 AMWG diagnostics package provided by NCAR and their corresponding datasets can
297 be found in the NCAR Climate Data Guide
298 ([https://climatedataguide.ucar.edu/collections/diagnostic-data-sets/ncar-doe-](https://climatedataguide.ucar.edu/collections/diagnostic-data-sets/ncar-doe-cesm/atmosdiagnostics)
299 [cesm/atmosdiagnostics](https://climatedataguide.ucar.edu/collections/diagnostic-data-sets/ncar-doe-cesm/atmosdiagnostics)). The time periods used to calculate the climatological means
300 are simply following the default setup of the AMWG diagnostics package.

301 We further evaluate the performance of the three macrophysics schemes by using the
302 approach of Su *et al.* [2013], which compares CF and CWC sorted by large-scale
303 dynamical and thermodynamic parameters. The CF products are based on the 2B-
304 GEOPROF R04 dataset [Marchand *et al.*, 2008], while the CWC data are based on the
305 2B-CWC-RO R04 dataset [Austin *et al.*, 2009]. The methodology from Li *et al.* [2012]
306 is used to generate gridded data. Two independent approaches (*i.e.*, FLAG and PSD
307 methods) are used in Li *et al.* [2012] to distinguish ice mass associated with clouds
308 from ice mass associated with precipitation and convection. The PSD method is used
309 in this study [Chen *et al.*, 2011]. Four years of CloudSat/CALIPSO data, from 2007 to
310 2010, are used to carry out the statistical analyses. These data are used to obtain overall
311 climatological means to compare to those obtained from model simulations instead of
312 undergoing rigorous year-to-year comparisons between observations and simulations.
313 Monthly data from ERA-Interim for the same four years are used to obtain the
314 dynamical and thermodynamic parameters used in Su *et al.*'s approach. These
315 parameters include large-scale vertical velocity at 500 mb and RH at several vertical
316 levels.

317

318 3.2 Offline calculation of cloud fraction

319 To evaluate the impact of assumptions of CF distributions for the RH- and PDF-
320 based schemes, we conducted offline calculations of the CF by using the reanalyzed
321 temperature, humidity, and condensate data from ERA-Interim. As the differences in
322 CF characteristics do not change from month to month, the results for July are shown

323 in Figure 2 as an example. The ERA-Interim reanalysis performed by Dee *et al.* [2011]
324 using a 0.75° resolution from 1979 to 2012 is used 410 in the calculation. With this
325 offline approach, we can observe the impacts of these macrophysics assumptions with
326 a balanced atmospheric state provided by the reanalysis.

327 Using the U_pdf of GTS scheme as an example to elaborate on the details of
328 calculation procedures, we simply obtain the cloud liquid mixing ratio (\bar{q}_l), water vapor
329 mixing ratio (\bar{q}_v), and air temperature (to calculate \bar{q}_{sl}) from the ERA-Interim as input
330 variables to calculate the liquid CF via using equations (6) and (4) when \bar{q}_l is greater
331 than 10^{-10} (kg kg^{-1}). When \bar{q}_l is smaller than 10^{-10} (kg kg^{-1}) and if $\text{RH} > \text{RH}_c$, CFs are
332 calculated based on equation (3) and the liquid CF parameterization of Sundqvist *et al.*
333 [1989] and if $\text{RH} < \text{RH}_c$, CFs are equal to zero. Ice CFs are calculated similarly as those
334 of liquid CFs but using equation (7), \bar{q}_i , \bar{q}_{si} , and $\text{sup} = 1.0$. Procedures for calculating
335 CFs diagnosed by the T_pdf of GTS scheme are similar to those of U_pdf but using
336 equation set of triangular PDF. Values of RH_c used in the U_pdf and T_pdf of GTS
337 schemes are assumed to be 0.8 and height-independent. Maximum overlapping
338 assumption is used to calculate the horizontal overlap between the liquid CF and ice CF.

339 Overall, the geographical distributions from the two GTS schemes are similar to that
340 of the ERA-Interim reanalysis shown in Figure 2. In July, high clouds corresponding to
341 deep convection are shown over South and East Asia where monsoons prevail. The
342 diagnosed clouds of the GTS scheme have a maximum level of 125 hPa, which is
343 consistent with those of the ERA-Interim reanalysis, but also have a more extensive
344 cloud coverage of up to 90%. Below the freezing level at approximately 500 hPa, the
345 CF diagnosed by the GTS scheme is comparable with that diagnosed by ERA-Interim
346 reanalysis. The most substantial differences in CF between the GTS scheme and the
347 ERA-Interim are observed in the mixed-phase clouds, such as the low clouds over the
348 Southern and Arctic Oceans. Such differences suggest that more complexity in
349 microphysics assumptions may be needed to describe the large-scale balance of mixed-
350 phase clouds. It is interesting to note that the U_pdf simulates CFs at the lower levels
351 in closer agreement with those of ERA-Interim and the U_pdf obtains similar
352 magnitude of CFs as those of the T_pdf at the upper levels. The potential reason resulted
353 in such differences could be related to the nature of the two PDFs. The U_pdf is likely
354 to calculate more CFs compared to T_pdf given similar RH and cloud liquid mixing
355 ratio in the lower atmospheric levels. The diagnosed CF for the Park macrophysics
356 scheme is also shown in the right column of Figure 2. We found that the cloud field
357 diagnosed by the Park macrophysics scheme was considerably different from that
358 diagnosed by ERA-Interim reanalysis and the GTS schemes. The Park scheme
359 diagnosed overcast high clouds of 100–125 hPa with coverage of up to 100% over the
360 warm pool and Intertropical Convergence Zone, but very little cloud coverage below

361 200 hPa, suggesting that the assumptions of the Park scheme are probably not suitable
362 for large-scale states of the ERA-Interim reanalysis.

363 However, such a calculation does not account for the feedback of the clouds to the
364 atmospheric states through condensation or evaporation and cloud radiative heating.
365 Therefore, we further extended our single-column CAM5.3 experiments to examine the
366 impact of the cloud PDF assumption.

367

368

369 4. Single-column results

370 This section presents the analysis of single-column simulations using the TWP-ICE
371 field campaign. We focused on the CF fields and humidity fields to see how the RH_c
372 assumption affects these features through humidity partitioning. Five sets of model
373 experiments were conducted. In addition to the T_pdf and U_pdf of the GTS and Park
374 schemes, we also include the T_pdf and U_pdf of the GTS scheme with the Slingo ice
375 CF parameterization. These experiments can help us to interpret the impacts of RH_c on
376 liquid and ice CFs separately.

377 Figure 3 shows the correlation between CF and RH for the three time periods during
378 the TWP-ICE. As expected, the correlation coefficients are quite similar for the
379 individual schemes during the active monsoon period when convective clouds
380 dominated ($R = 0.73$, Park, vs. 0.71 , T_pdf, vs. 0.70 , U_pdf). In contrast, the correlation
381 coefficient between CF and RH differs during the suppressed monsoon period when
382 stratiform clouds dominated ($R = 0.47$, Park, vs. 0.71 , T_pdf, vs. 0.76 , U_pdf). The
383 correlation coefficient between CF and RH is approximately 20% higher for the
384 stratiform-cloud-dominated period when using T_pdf or U_pdf in the GTS scheme. It
385 is also worth mentioning that, during the monsoon break period when both convective
386 and stratiform clouds co-exist, the usage of the GTS scheme can also increase the
387 correlation between CF and RH by 10% compared to the default Park scheme. Notably,
388 the higher correlation coefficient for stratiform-cloud-dominated areas only suggests
389 that the GTS scheme can somehow better simulate the variation of CF associated with
390 RH, for which stratiform cloud macrophysics parameterization normally takes effect in
391 CAM5.3.

392 Comparisons between T_pdf with the Slingo ice CF and the Park scheme can be used
393 to examine the role of applying a PDF-based approach in simulating the liquid CF in
394 the GTS scheme. The use of a PDF-based approach for calculating the liquid CF can
395 increase the correlation between CF and RH by approximately 12% during the
396 suppressed monsoon period ($R = 0.69$, T_pdf with Slingo, vs. 0.47 , Park). Such an
397 outcome also suggests that implementing a PDF-based approach for liquid clouds can
398 lead to more reasonable fluctuations between CF and RH in GCM grids.

399 It turns out that using the PDF-based approach for ice clouds slightly contributes to
400 the increased correlation between CF and RH, as shown in Figure 3 with the T_pdf
401 scheme ($R = 0.69$, T_pdf with Slingo, vs. 0.71 , T_pdf) or U_pdf scheme ($R = 0.73$,
402 U_pdf with Slingo, vs. 0.76 , U_pdf). Such results also suggest that extending this PDF-
403 based approach for ice clouds can better simulate changes in the cloud ice fraction using
404 an RH-based approach rather than an RH_c -based approach. Notably, such pair
405 comparisons (*i.e.*, T_pdf with Slingo cloud ice fraction scheme vs. T_pdf and vs. Park)
406 only reveal the important features of the GTS scheme, such as how variations in liquid
407 CF are better correlated with changes in RH of the GCM grids when compared to that
408 of the default cloud macrophysics scheme. In fact, such high correlations between CF
409 and RH seen in the GTS and Park schemes are not consistent with those of observations
410 as shown in Figure 3(a), suggesting that, in nature, CF and RH is likely to be non-linear.

411 Admittedly, it is not easy to directly use the observational CF of TWP-ICE field
412 campaign to evaluate the performances of stratiform cloud macrophysics schemes in
413 the SCAM simulations due to the co-existing of other CF types determined by the deep
414 and shallow convective schemes as well as cloud overlapping treatments in both
415 horizontal and vertical directions. As expected, correlation coefficients between the
416 simulated and observed CFs are not high and their values do not differ a lot among the
417 five cloud macrophysics schemes (Table S1).

418 To minimize possible interference from deep and shallow convective CFs, we picked
419 up the stratiform cloud-dominated levels and time period to examine the CF-RH
420 distributions. Figure 4 shows scatter plots of RH and CF between 50 and 300 hPa
421 determined from observations [Xie *et al.*, 2010] and simulated by models run for the
422 suppressed monsoon period from the TWP-ICE case. It turns out that the CF-RH
423 distributions simulated by the GTS schemes (Figures 4(c) and 4(f)) are closer to those
424 of the observational results (Figure 4(a)) except under more overcast conditions (*i.e.*,
425 $RH > 70\%$ and $RH > 110\%$). In contrast, the CF-RH distributions simulated by the Park
426 scheme are much less consistent with those of observations (Figures 4(d) vs. 4(a)). On
427 the other hand, by excluding PDF-based treatment for the cloud ice fraction in the GTS
428 scheme, a more obvious spread in the CF-RH distribution is produced (comparing
429 Figures 4(b) and 4(c) or Figures 4(e) and 4(f)). In other words, the comparisons shown
430 in Figure 4 suggest that applying a PDF-based treatment for both liquid and ice CF
431 parameterizations can simulate the CF-RH distributions in better agreements with the
432 observational results.

433

434

435 5. Global-domain results

436 5.1 Impacts on cloud fields

437 a. Cloud fraction

438 In Figure 5, total CF simulated by the GTS schemes and the CESM default cloud
439 macrophysics scheme, obtained from the COSP satellite simulator of the AMWG
440 package of NCAR CESM, are compared with the total CF in CALIPSO-GOCCP.
441 Notably, the following comparisons for the CF and associated variables are not only
442 affected by the changes in the cloud macrophysics but also contributed by the deep and
443 shallow convective schemes as well as cloud overlapping assumptions in the horizontal
444 and vertical directions. Both global mean and root-mean-square error (RMSE) values
445 are improved by applying U_pdf in the GTS scheme. The CF simulation resulting from
446 the use of U_pdf in the GTS scheme is qualitatively similar to that of
447 CloudSat/CALIPSO, especially over the mid- and high-latitude regions and for the
448 annual and December-January-February (DJF) simulations (Figure 6). On the other
449 hand, the results of the Park scheme show clouds at higher altitudes in the tropics in
450 closer agreement with CloudSat/CALIPSO than those of U_pdf or T_pdf. Cross-section
451 comparison of the zonal height shows that the CF simulation using U_pdf and T_pdf in
452 the GTS scheme agrees better with that of CloudSat/CALIPSO than that produced by
453 Park under most scenarios (globally, within 60° N–60° S, and within 30° N–30° S),
454 especially for the annual and DJF simulations (Table 1). In contrast, some scenarios
455 show lower RMSEs when the Park scheme is used, *e.g.*, for the June-July-August (JJA)
456 season globally, within 30–90° N, and within 30–90° S. Interestingly, when high
457 latitudes are included (*i.e.*, 30–90° N and 30–90° S), U_pdf still results in the smallest
458 RMSE values, except for during the JJA season. It is evident that some CFs are existing
459 at the upper level in the Antarctic in JJA when U_pdf or T_pdf of GTS is used. However,
460 such high CFs are not seen in CloudSat/CALIPSO observations, suggesting that the
461 usage of GTS schemes could cause significant biases in CFs under such environmental
462 conditions. This is of course highly related to the ice CF schemes of GTS. More
463 observation-constrained adjustments or tuning of the ice CF schemes of GTS are
464 needed to reduce the biases in CFs in similar atmospheric environments like the upper
465 level of the Antarctic winter. Potential tuning parameters of ice CF scheme of GTS are
466 *sup* and *RH_c* which are discussed in Section 5.7c.

467 We also compared the annual latitude–longitude distributions of CF at different
468 specific pressure levels (Figure 7). The use of U_pdf resulted in a CF simulation
469 relatively similar to that of CloudSat/CALIPSO for mid-level clouds, *i.e.*, 300–700 mb,
470 particularly for the mid- and high latitudes. However, none of the CF parameterizations
471 are able to simulate stratocumulus clouds effectively, as revealed at the 850 and 900 mb
472 levels. For high clouds, the GTS and Park schemes exhibit observable differences
473 regarding the maximum CF level. Table 2 summarizes the RMSE values for the
474 latitude–longitude distribution of CFs at nine specific levels for the three schemes and

475 CloudSat/CALIPSO for the annual, JJA, and DJF means. For the annual mean, U_pdf
476 results in the smallest RMSE at all levels except at 125 mb, for which the Park scheme
477 yields the smallest RMSE (Table 2). For JJA, the Park scheme is closer to the
478 observations aloft (100–200 mb) and nearest the surface (900 mb). For DJF, U_pdf
479 again performs best at most levels except 100 and 125 mb, for which T_pdf is slightly
480 better, while for JJA, U_pdf is only best for most of the levels below 300 mb. Overall,
481 U_pdf in the GTS scheme results in better latitude–longitude CF distributions for 300–
482 900 mb for the annual, DJF, and JJA means, suggesting improvements in CF simulation
483 for middle and low clouds.

484 When annual, DJF, and JJA mean vertical CF profiles are averaged over the entire
485 globe and between 30° N and 30° S, U_pdf in the GTS scheme can produce a global
486 simulation close to that of CloudSat/CALIPSO for 200–850 mb (Figure S1). In contrast,
487 there is a large discrepancy between the simulated and observed CFs over the tropics.
488 Although the GTS schemes can simulate CF profiles above 100 mb, the height of the
489 maximum CF is lower than that of CloudSat/CALIPSO. In contrast, the height of the
490 maximum CF simulated by the Park scheme is similar to that of CloudSat/CALIPSO
491 but overestimated in CF. As before, when compared with CloudSat/CALIPSO, U_pdf
492 in the GTS scheme results in the smallest RMSE and the largest correlation coefficient
493 of the three schemes, whether or not the lower levels are included except in JJA at 125
494 mb, for which Park yields the smallest RMSE (Table S2). The reason for excluding the
495 lower levels from the statistical results is that there may be a bias for low clouds
496 retrieved by CloudSat due to radar-signal blocking by deep convective clouds.

497 The different degrees of changes for the global and tropical CFs can be attributed to
498 the relative roles of cumulus parameterizations (both deep and shallow) and stratus
499 cloud macrophysics/microphysics for the different latitudinal regions. It is expected that
500 the GTS scheme can alter CF simulations in the mid- and high-latitude areas more than
501 in the tropics because more stratiform clouds occur in those areas. It is also interesting
502 to note that, although it is known that more convective clouds exist in the tropics (*i.e.*,
503 the cumulus parameterization contributes more to the grid CF), the GTS scheme can
504 also affect the CF simulation over the tropics to some extent.

505

506 b. Cloud fraction and cloud water content

507 In Figures 8 and 9, the distributions of CWC and CF as functions of large-scale
508 vertical velocity at 500 mb (ω_{500}) or mean RH averaged between 300 and 1000 mb
509 (RH_{300–1000}) are evaluated against CloudSat/CALIPSO observations for 30° N–
510 30° S and 60° N–60° S. Figures 8 and 9 show that the model simulations are all
511 qualitatively more similar to each other than to the observations. Further statistical
512 comparisons are shown in Table 3. It is encouraging to note that, in addition to the slight

513 improvements in CF for both of these latitudinal ranges, the use of U_pdf in the GTS
514 scheme results in a CWC simulation that is more consistent with CloudSat/CALIPSO,
515 whether it is plotted against ω_{500} or RH300–1000. The RMSE and correlation
516 coefficient (R) values in Table 3 confirm this. For global simulations, using U_pdf also
517 results in better agreement with CloudSat/CALIPSO for both CF and CWC when they
518 are plotted against ω_{500} , although for CWC plotted against RH300–1000, the Park
519 scheme yields the smallest RMSE (Table 3). Overall, these comparisons yield results
520 that are consistent with the general characteristics of most CMIP5 models, as found by
521 Su *et al.* [2013]. GCMs in general simulate the distribution of cloud fields better with
522 respect to a dynamical parameter as opposed to a thermodynamic parameter.

523 It is also worth noting that the use of U_pdf yields a 20–30% improvement in R when
524 plotted against RH300–1000 for the two latitudinal ranges, 30° N–30° S and 60° N–
525 60° S. The observable improvement in a thermodynamic parameter is an indication of
526 the uniqueness of this GTS scheme, in that it is capable of simulating the variation in
527 cloud fields relative to that in RH fields. There are also slight improvements in cloud
528 fields with respect to large-scale dynamical parameters. On the other hand, the Park
529 scheme results in an approximately 20% improvement in R when plotted against
530 RH300–1000 for the global domain, suggesting that the default Park scheme still
531 simulates cloud fields better over the high latitudinal regions. It is thus worth addressing
532 the likelihood that the different CF and CWC results for the different latitudinal ranges
533 simulated using the GTS scheme induce cloud–radiation interactions distinct from
534 those simulated in the Park scheme. Such changes in cloud–radiation interactions would
535 not only modify the thermodynamic fields but also the dynamic fields in the GCMs.
536 These changes are in turn likely to affect the climate mean state and variability. We
537 assess and compare these potential effects in the following subsection.

538

539 5.2 Effects on annual mean climatology

540 GTS schemes tend to produce smaller RMSE values for most of the global mean
541 values of the radiation flux, cloud radiative forcing, and CF parameters shown in Table
542 4, suggesting that the GTS scheme is capable of simulating the variability of these
543 variables. Furthermore, the assumed U_pdf shape appears to perform better for
544 outgoing longwave radiation flux, longwave cloud forcing (LWCF), and CF at various
545 levels, whereas the T_pdf assumption is better for simulating net and shortwave
546 radiation flux at the top of the atmosphere as well as shortwave cloud forcing (SWCF)
547 (Table 4). On the other hand, the Park scheme is better for simulating clear-sky net
548 shortwave radiation flux and precipitation. Smaller RMSE values can also be seen for
549 parameters such as total precipitable water, total-column cloud liquid water, zonal wind
550 at 200 mb (hereafter, U_200), and air temperature at 200 mb (hereafter, T_200) when

551 U_pdf of GTS is used. For global annual means, U_pdf simulates net radiation flux at
552 the top of the atmosphere, all- and clear-sky outgoing longwave radiation flux, and
553 precipitable water as well as U_200 and T_200 are in closer agreement with
554 observations. In contrast, the Park scheme is better for simulating global mean variables
555 such as net shortwave radiation flux at the top of the atmosphere, longwave cloud
556 forcing, and precipitation. T_pdf simulates SWCF closest to the observational mean.

557 Overall, the averaged RMSE values of the ten parameters are 0.97 and 0.96 for U_pdf
558 and T_pdf, respectively, in the GTS schemes (Figure 10), suggesting that using the GTS
559 schemes would result in global simulation performances more or less similar to those
560 from the Park scheme. It is also worth noting that the biases in RH are smallest when
561 U_pdf in the GTS scheme is used (Table S3 of the supplementary material). In contrast,
562 T_pdf results in the smallest biases for SWCF, sea-level pressure, and ocean rainfall
563 within 30° N–30° S. On the other hand, the Park scheme produces the smallest biases
564 regarding mean fields such as LWCF, land rainfall within 30° N–30° S, Pacific surface
565 stress within 5° N–5° S, zonal wind at 300 mb, and temperature.

566 Comparisons of latitude–height cross-sections of RH and ERA-Interim show that the
567 GTS schemes tend to simulate RH values smaller than the default scheme does,
568 especially for high-latitude regions (> 60° N and 60° S), as shown in Figure 11. In
569 general, in terms of RH, using T_pdf in the GTS scheme results in better agreement
570 with ERA-Interim (Table S4). Figure 12 shows that the Park and T_pdf schemes are
571 wetter than ERA-Interim almost everywhere and that the uniform scheme is sometimes
572 drier. Table S5(a) further suggests that specific humidity simulated by the GTS schemes
573 is slightly more consistent with ERA-Interim than the Park scheme. Comparisons of air
574 temperature show that the three schemes tend to have cold biases almost everywhere.
575 However, it is interesting to note that the cold biases are reduced to some extent while
576 using the GTS schemes compared to the default scheme, as is evident in the smaller
577 values of RMSE shown in Table S5(b). These effects on moisture and temperature are
578 likely to result in changes in the annual cycle and seasonality of climatic parameters.
579 Such observable changes in RH, clouds (both CF and CWC), and cloud forcing suggest
580 that the GTS scheme will simulate cloud macrophysics processes in GCMs quite
581 differently from the Park scheme, owing to the use of a variable-width PDF that is
582 determined based on grid-mean information.

583

584 5.3 Changes in the annual cycle of climatic variables

585 Figure 13 shows the annual cycle of precipitable water simulated by the three
586 schemes. The magnitude of precipitable water simulated by the GTS schemes is closer
587 to the ERA-Interim data than the Park simulation is (Table S6). Interestingly, U_pdf
588 results in slightly better agreement with ERA-Interim than T_pdf for the region 60° N–

589 60° S. This implies that the GTS scheme would alter the moisture field for both RH and
590 precipitable water in GCMs. These results are relatively more realistic with respect to
591 both the moisture field and CF and CWC (Figures 8 and 9) and are likely to yield a
592 more reasonable cloud–radiation interaction in the GCMs. It is therefore also worth
593 examining any differences in dynamic fields, for example, in the annual U₂₀₀ cycle,
594 between the three schemes and the ERA-Interim data (Figure 14). Like the annual cycle
595 of precipitable water, U₂₀₀ simulated by the GTS schemes is closer to that of ERA-
596 Interim than that simulated by the Park scheme, as supported by the smaller RMSE
597 shown in Table 8. Furthermore, the U_{pdf} assumption results in a better annual U₂₀₀
598 cycle than the T_{pdf} assumption, especially for 60° N–60° S. This further supports the
599 argument that this GTS scheme can effectively modulate global simulations, with
600 respect to both thermodynamic and dynamical climatic variables.

601 Figure 15 displays the global mean annual cycles of several parameters simulated by
602 the three schemes and the corresponding parameters from observational data. The GTS
603 scheme simulations of total precipitable water (TMQ) are close to that of ERA-Interim;
604 indeed, U_{pdf} almost exactly reproduces the ERA-Interim TMQ. However, we must
605 admit that such good agreement of the global mean is partly due to offsetting wet and
606 dry differences from ERA-Interim. The GTS schemes also produce a more reasonable
607 global mean annual cycle for outgoing longwave radiation (FLUT). It is probably due
608 to the reduced CF simulated by the GTS scheme compared to the Park scheme even
609 though the cloud top heights simulated by GTS are lower than observations in the
610 tropics. Interestingly, for SWCF, T_{pdf} yields a simulation closer to the observations
611 than the other two schemes, which is consistent with the features of the global annual
612 mean of SWCF shown in Figure 10 and Table S3. However, for LWCF, the annual cycle
613 simulated by Park is closest to the observations. The U_{pdf} of the GTS scheme also
614 results in improvements in U₂₀₀ and T₂₀₀ (Figure 15). The RMSEs for all of these
615 comparisons confirm these results (Table S7).

616

617 5.4 Changes in cloud–radiation interactions

618 As mentioned in Section 5.1, usage of the GTS cloud macrophysics schemes would
619 affect the cloud fields, *i.e.*, CF and CWC. This, in turn, is likely to affect global
620 simulations with respect to both mean climatology and the annual cycles of many
621 climatic parameters (as discussed in Sections 5.2 and 5.3) through cloud–radiation
622 interactions. Figure 16 compares CF, radiation heating rate (*i.e.*, longwave heating rate
623 plus shortwave heating rate, hereafter QRL+QRS) and temperature tendencies due to
624 moist processes (hereafter, DTCOND) for each pair-wise combination of the three
625 schemes. Qualitatively consistent changes in CF are apparent for the GTS schemes, *e.g.*,
626 an increase in the highest clouds over the tropics and a decrease below them, a decrease

627 in 150–400 mb clouds over the mid-latitudes, a decrease in 300–700 mb clouds over
628 the high latitudes, an increase in 300–700 mb clouds over the tropics to mid-latitudes,
629 and an increase in low clouds over the high-latitude regions. The GTS schemes also
630 yield a significant increase in CF at atmospheric levels higher than 300 mb over the
631 high-latitude regions (Figure 16). These changes affect the radiation calculations to
632 some extent. In addition, CWC is also affected by the GTS schemes (Figures 8 and 9).
633 The combined effects of the changes in CF and CWC are likely to result in changes in
634 cloud–radiation interactions. In addition, although there are significant changes in CF
635 at high atmospheric levels in the high-latitude regions, the combined effect of CF and
636 CWC on QRL+QRS is quite small, owing to the low CWC values over this region. The
637 changes in moisture processes, *i.e.*, DTCOND (Figure 16), also suggest that the
638 combined effects of the changes in the thermodynamic and dynamical fields occur as a
639 result of changes in cloud–radiation interactions within the GCMs from GTS schemes.

640 The bottom panel in Figure 16 shows the differences in CF, QRL+QRS, and
641 DTCOND between the two GTS schemes. Relative to T_pdf, U_pdf simulates a greater
642 CF for 300–1000 mb clouds within 60° N–60° S, but a smaller CF for all three cloud
643 levels for the high-latitude regions. Furthermore, the CWC vertical cross-section also
644 differs for the two GTS schemes (data not shown for limitations of space). Combining
645 the changes in CF and CWC, the corresponding changes in QRL+QRS and DTCOND,
646 particularly the increase of low clouds over the mid-latitude region, are clear with an
647 obvious decrease of high clouds over the tropical to mid-latitude region. It is also
648 evident that DTCOND simulated by the U_pdf is stronger than that simulated by the
649 T_pdf below 700 hPa. Such enhanced condensation heating is probably contributed by
650 the enhanced shallow convection as a result of changes in cloud-radiation interactions.
651 However, more process-oriented diagnostics are needed to understand the complicated
652 interactions of the moist processes.

653 Observable changes in large-scale circulations are likely, given the various changes
654 in QRL+QRS and DTCOND resulting from applying different cloud macrophysics.
655 Accordingly, both the mean and variability of the climate simulated by the GCMs differ
656 among the three schemes, as shown in the previous subsections. These results
657 emphasize the importance of improving cloud-related parameterization to provide
658 better simulations of the cloud–radiation interaction within GCMs. Furthermore, as
659 previously shown, the cloud–radiation interaction is highly sensitive to the assumptions
660 of the CF parameterization used in the macrophysical scheme in the GCMs, even if
661 there is only a small change in the CF parameterization. The uniqueness of the GTS
662 scheme is in its application of a variable PDF width to calculate CF in the default PDF-
663 based CF scheme of the CESM model. Further systematic experiments are necessary to
664 improve our understanding of the sensitivity of the GTS scheme, and some are

665 presented in Section 5.7.

666

667 5.5 Consistent changes in cloud radiative forcing, cloud fraction, and cloud condensates

668 Observable changes in clouds and radiation fluxes after adopting the GTS scheme
669 were clearly shown in the previous subsections. It is thus worth examining features in
670 cloud radiative forcings caused by the GTS scheme that produce such changes, as
671 compared to those of the default Park scheme. Figure 18 shows the difference in total
672 cloud fraction, SWCF, LWCF, CF, and averaged cloud water contents, as well as the
673 averaged RH at the three levels i.e., 100–400, 400–700, and 700–1000 mb, derived
674 from the T_pdf of GTS with the Park results subtracted. One can readily observe that
675 changes in SWCF (Figure 17(b)) are quite consistent with those for total CF, showing
676 a decrease in the total CF over the area within 30° N and 30° S with an increase
677 everywhere else (Figure 17(a)). Such prominent changes in latitudinal distribution of
678 SWCF can be further related to the changes in the low (Figure 17(e)) and middle (Figure
679 17(f)) CFs particularly associated with low clouds.

680 On the other hand, changes in the high CF (Figure 17(d)) are also quite consistent
681 with those in LWCF (Figure 17(c)), showing an overall decrease of high clouds
682 especially over the tropical convection areas. As expected, changes in cloud water
683 condensates (Figures 17(g)–(i)) are closely related to changes in the CF at the three
684 levels except for the middle clouds. Therefore, according to the evidence shown in
685 Figures 17(a)–(i), it is clear that use of the GTS scheme would cause significant changes
686 in the spatial distribution of low, middle, and high clouds (both in CF and cloud water
687 condensates) that would result in corresponding changes in cloud radiative forcings
688 (both for SWCF and LWCF).

689 Surprisingly, changes in RH at the three levels (Figures 17(j)–(l)) are relatively less
690 consistent with changes in the CF and condensates, especially for middle and low
691 clouds over the mid- and high-latitude areas. Such results also indicate that there are
692 complicated factors accounting for changes in RH in the GCMs. We suggest that, in
693 addition to the active roles of the GTS scheme in redistributing/modulating moisture
694 between clouds (*i.e.*, cloud liquid or ice) and environment (water vapor) in GCM grids,
695 thermodynamic and dynamical feedback resulting from cloud–radiation interactions
696 also contribute to RH changes. At the present stage, we cannot quantify these individual
697 contributions. More in-depth analysis is needed to unveil the detailed mechanisms of
698 why GTS schemes tend to produce less low clouds over the tropics while more low
699 clouds over the mid- and high latitudes compared to the default Park scheme, as well
700 as observable changes regarding middle and high clouds.

701

702 5.6 Discussions on causality resulted from the GTS scheme

703 Admittedly, it is challenging to disentangle the relationship between causes and
704 effects resulted from the usage of the GTS scheme in the global simulations. As shown
705 in the previous section, utilizing GTS schemes yield changes in cloud fields (both CF
706 and CWC) and cloud radiative forcings. Mean climatology and the annual cycles of
707 many climatic parameters (as discussed in Sections 5.2 and 5.3) are changed to some
708 extent through the cloud–radiation interactions. Notably, such changes in cloud fields
709 are not only contributed by the stratiform cloud macrophysics scheme but also affected
710 by other moist processes in GCMs (*e.g.*, deep convection, shallow convection,
711 stratiform cloud microphysics, and turbulent boundary layer schemes). Moreover,
712 cloud overlapping assumptions in the macrophysics scheme of CESM (both in the
713 horizontal and vertical directions) also affect the global simulation results through
714 changes in thermodynamic and dynamic fields caused by utilizing different cloud
715 macrophysics schemes.

716 We suggest that those asymmetric changes in total CF, SWCF, and LWCF between
717 the tropics and the mid- and high latitudes (Figure 17) could be related to regions where
718 stratiform cloud macrophysics parameterization takes effect more compared to other
719 moist parameterizations in the physical-process splitting framework of CESM. Such
720 asymmetric changes in cloud radiative forcing are in turn likely to affect the climate
721 mean state and atmospheric circulation. More so-called process-oriented analyses and
722 simulation designs can be devoted to unveiling the causality resulted from the GTS
723 scheme. For example, detailed output of tendency terms of moist processes of GCMs
724 can be useful to investigate how individual moist process responses to the perturbations
725 caused by the GTS scheme and interact together to produce those different changes in
726 low, middle and high clouds.

727

728 5.7 Uncertainty in GTS cloud fraction parameterization

729 a. Assumption of PDF shape in the GTS scheme

730 In general, the simulations of CF, RH, and other parameters (*e.g.*, global annual mean
731 and/or annual cycle) using the T_pdf scheme that have been discussed and illustrated
732 thus far have distribution features qualitatively and values quantitatively between those
733 of the Park and U_pdf schemes. In other words, the characteristics of the T_pdf
734 simulations are a combination of those from both the default Park scheme and the
735 U_pdf scheme. This is to be expected because there are fewer differences between the
736 Park and T_pdf schemes than between the Park and U_pdf schemes in terms of cloud
737 macrophysics parameterization. Since the shape of the PDF is triangular for both the
738 Park and T_pdf schemes, the only difference between these two is that T_pdf has a
739 variable PDF width that is based on the grid-mean mixing ratio of hydrometeors and
740 the saturation ratio of the atmospheric environment, rather than the fixed-width function

741 of RH_c . Even such a minor difference, however, can have an impact on both the
742 thermodynamic and dynamical fields in global simulations. Our findings further
743 suggest that the use of a variable PDF width to determine CF results in some changes
744 in consistency between the RH and CF fields, as well as in the simulation of SWCF and
745 net radiation flux at the top of atmosphere. As mentioned in Section 1, a diagnostic
746 approach to determining the triangular PDF width of the default Park scheme can be
747 used to refine the Park scheme [Appendix A of Park *et al.*, 2014]. This is effectively the
748 same as using the GTS scheme with T_pdf.

749 However, it is also evident that assuming a uniform PDF (*i.e.*, a rectangular shape)
750 can have a larger effect on global simulations, as seen with our use of U_pdf. It is
751 interesting to note that the use of U_pdf yields a smaller overall RMSE for many
752 thermodynamic and dynamical fields than does the use of T_pdf. This implies that a
753 uniform distribution is probably more appropriate for the 2° horizontal resolution
754 currently used in global simulations. The scale-dependence of the PDF shape is
755 certainly important to consider, as revealed in our comparisons between T_pdf and
756 U_pdf, but this is beyond the scope of this paper. Furthermore, the possible dependence
757 of PDF shape on specific cloud systems in different regions should also be examined
758 using systematic tests and simulation designs.

759

760 b. Uncertainty resulting from cloud-ice fraction parameterization

761 It is worth evaluating the possible uncertainty related to CF for cloud ice because the
762 saturation adjustment assumption used for cloud liquid may not apply to cloud ice, as
763 discussed in Section 1. We thus examine the sensitivity of the super-saturation values
764 for the ice CF by multiplying by q_{si} , as shown in equation 7 by the constant *sup*. Several
765 values of *sup* are assumed for the ice CF in the GTS schemes with CF simulated using
766 Slingo's approach to parameterization as used by Park *et al.* [2014] and are compared
767 with the CloudSat/CALIPSO observational data (Figure S5). Both GTS schemes are
768 sensitive to the *sup* value. For U_pdf, CF decreases more-or-less linearly with
769 increasing *sup* values, but there is no such clear linearity for T_pdf, especially for *sup*
770 values of 1.0000–1.0005. Interestingly, changing the *sup* value for the ice CF affects
771 the liquid CF results for the scheme. We also find that the CF profile simulated by
772 U_pdf when *sup* = 1.0005 is similar to that simulated using Slingo's approach to
773 parameterization, especially for middle and low clouds. Based on these sensitivity tests,
774 it is evident that the *sup* value used in the ice CF formulae of the GTS scheme can be
775 regarded as a tunable parameter under the present cloud macrophysics and
776 microphysics framework of the CESM model. When *sup* = 1.0 in the GTS scheme with
777 U_pdf, the results are comparable to CloudSat/CALIPSO observations, while with
778 T_pdf, the *sup* value can be tuned between 1.0 and 1.005 to mimic the

779 CloudSat/CALIPSO data (Figure S5). Thus, the results of GTS schemes are sensitive
780 to the supersaturation threshold and suggest that it is still quite challenging to produce
781 a reasonable parameterization for the ice CF, given the longer time-scales needed for
782 ice clouds to reach saturation equilibrium.

783

784 c. Tuning parameters of the GTS scheme

785 The top of atmosphere (TOA) radiation balance is very important for a coupled
786 climate model and modifying cloud-related physical parameterizations can
787 significantly alter the TOA radiation balance. It is thus worth comparing the difference
788 in TOA radiation flux between the GTS and the default Park schemes as listed in Table
789 4. It turns out that the net TOA radiation of T_pdf is smaller than that of the Park scheme
790 by 0.93 W m^{-2} . In contrast, the net TOA radiation of U_pdf is smaller than that of the
791 Park scheme by 5.24 W m^{-2} . We can expect that utilizing U_pdf of the GTS scheme
792 will introduce much stronger TOA radiation imbalance compared to T_pdf of the GTS
793 scheme in present physical parameterization framework of NCAR CESM 1.2.2. Our
794 past experiences in tuning GCMs also show that implementing strong tuning sometimes
795 will indeed offset the improvements resulted from physical parameterizations with less
796 tuning. In fact, to avoid the situation, we used the T_pdf of GTS scheme (with tuning
797 as discussed below) as the stratiform cloud macrophysics scheme of TaiESM model for
798 participating the CMIP6 project [Lee *et al.*, 2020].

799 As mentioned in the previous subsection, the *sup* value can be tuned and CF profiles
800 would be modified accordingly as shown in Figure S5. It is thus worth discussing the
801 sensitivity of tuning parameters of the GTS scheme and whether such tuning would
802 affect overall model performance. It is interesting to note that, although significant
803 changes in CF profiles (Figure S5), SWCF, and LWCF (Table S8) between *sup* = 1.0
804 and *sup* = 1.05 are shown, differences in net radiation at the top of model (RESTOM)
805 between *sup* = 1.0 and *sup* = 1.05 are only about 0.6 to 0.7 W m^{-2} for the GTS schemes
806 (Table S8). Such outcome suggests that possible compensating effects exist between
807 changes in SWCF and LWCF associated with cloud overlapping. One could expect that,
808 despite relatively smaller changes in RESTOM, significant changes in SWCF and
809 LWCF between *sup* = 1.0 and *sup* = 1.05 could potentially affect the overall
810 performance of GCMs. Comparisons of Taylor diagrams and biases confirm this
811 (Figures S6 and S7, Table S9). Notably, *sup* here is assumed to be a constant and height-
812 independent. Further height-dependent tuning can be tested.

813 In addition, RH_c of cloud macrophysics parameterizations are frequently used to tune
814 the radiation balance issue of coupled GCMs. As mentioned in section 2.1, although
815 RH_c is no longer used once clouds formed in the GTS schemes, the GTS schemes still
816 need RH_c when clouds start to form. RH_c is assumed to be 0.8 and height-independent

817 in this study. Our past tuning experiences suggest that tuning RH_c of GTS scheme could
818 moderately alter the net radiation flux at TOA of coupled global simulations. For
819 example, the net radiation fluxes at TOA are -0.61 and -0.23 W m^{-2} for $RH_c = 0.83$ and
820 $RH_c = 0.85$, respectively, in TaiESM tuning work using T_pdf of GTS scheme.
821 Therefore, RH_c in the GTS scheme can be one of the parameters for tuning GCMs.
822 Moreover, height-dependent RH_c as that of the Park cloud macrophysics scheme can be
823 considered to tune the TOA radiation balance.

824

825

826 6. Conclusions

827 In this paper, we presented a macrophysics parameterization based on a probability
828 density function (PDF) called the GFS-TaiESM-Sundqvist (GTS) cloud macrophysics
829 scheme, which is based on Sundqvist's cloud macrophysics concept for global models
830 and the recent modification of the cloud macrophysics in the NCAR CESM model by
831 Park *et al.* [2014]. The GTS scheme especially excludes the assumption of a prescribed
832 critical relative humidity threshold (RH_c), which is included in the default cloud
833 macrophysics schemes, by determining the width of the PDF based on grid
834 hydrometeors and saturation ratio.

835 We first used ERA-Interim reanalysis data to examine offline the validity of the
836 relationship between cloud fraction (CF) and relative humidity (RH) based on the PDF
837 assumption. Results showed that the GTS assumption better describes the large-scale
838 equilibrium between CF and environment conditions. In a single-column model setup,
839 we noticed, according to the pair-wise comparisons shown and discussed in Figures 3
840 and 4, the use of PDF-based treatments for parameterizing both liquid and ice CFs in
841 the GTS schemes contributed to the CF-RH distributions. The GTS schemes simulated
842 the CF-RH distributions closer to those of the observational results compared to the
843 default scheme of CAM5.3.

844 According to our detailed comparisons with observational cloud field data (CF and
845 cloud water content (CWC)) from CloudSat/CALIPSO, GTS parameterization is able
846 to simulate changes in CF that are associated with changes in RH in global simulations.
847 Improvements with respect to the CF of middle clouds, the boreal winter, and mid- and
848 high latitudes are particularly evident. Furthermore, examination of the vertical
849 distributions of CF and CWC as a function of large-scale dynamical and
850 thermodynamic parameters suggests that, compared to the default scheme, simulations
851 of CF and CWC from the GTS scheme are qualitatively more consistent with the
852 CloudSat/CALIPSO data. It is particularly encouraging to observe that the GTS scheme
853 is also capable of substantially increasing the pattern correlation coefficient of CF and
854 CWC as a function of a large-scale thermodynamic parameter (*i.e.*, RH300–1000).

855 These effects appear to have a substantial impact on global climate simulations via
856 cloud–radiation interactions.

857 The fact that CF and CWC simulated by the GTS scheme are temporally and spatially
858 closer to those of the observational data suggests that not only the climatological mean
859 but also the annual cycles of many parameters would be better simulated by the GTS
860 cloud macrophysical scheme. Improvements with respect to thermodynamic fields such
861 as upper-troposphere and lower-stratosphere temperature, RH, and total precipitable
862 water were more substantial even than those in the dynamical fields. This was
863 consistent with our comparisons based on the vertical distribution of CF and CWC as
864 functions of large-scale dynamical and thermodynamic forcing. Interestingly, the GTS
865 scheme results in observable changes in the annual cycle of zonal wind at 200 hPa,
866 which suggests that the modification of thermodynamic fields resulting from changes
867 in cloud–radiation interactions will, in turn, reciprocally affect the dynamical fields.
868 Accordingly, it is worth investigating possible changes in large-scale circulation,
869 monsoon evolution, and short- and long-term climate variability in future research.

870 GTS schemes can simulate spatial distributions of cloud radiative forcings (both for
871 shortwave and longwave) quite differently compared to the default Park scheme.
872 Changes in cloud radiative forcings are very consistent with different latitudinal
873 changes in CF and cloud water condensates at the three cloud levels. The most
874 important feature of the GTS scheme is that CF is self-consistently determined based
875 on hydrometeors and the environmental information in the model grid box in the
876 general circulation model (GCM) simulation. In contrast to the prescribed vertical
877 profile of RH_c used in many current GCMs, the width of the PDF in the GTS scheme is
878 variable and calculated in a diagnostic way. A fixed RH_c is thus no longer used once
879 clouds are formed. This feature also potentially makes the GTS scheme a candidate
880 macrophysics parameterization for use in modern global weather forecasting and
881 climate prediction models as it better simulates the CF-RH relationship. However,
882 further efforts are required to develop a more meaningful and physical way to
883 parameterize the super-saturation ratio assumption applied to the cloud ice fraction in
884 the GTS scheme, and to investigate why a uniform PDF in the GTS scheme performs
885 better overall than the triangular PDF.

886

887 Appendix A

888 Derivations of cloud fraction and half width of triangular PDF

889 We used the triangular distribution instead of the uniform distribution to diagnose the cloud fraction.

890 The triangular PDF of total water substance q_t is now assumed to be triangular distribution with a
891 width of δ (Fig. 1b) with the saturated part being the cloudy region. Following the hint of *Park et al.*
892 [2014] and *Tompkins* [2005], we performed a variable transform by substituting q_t with $s = (q_t -$

893 $\bar{q}_t)/\delta$.

894 Thus, the original probability distribution becomes a triangular distribution $P(q_t)$ with a unit half
895 width and variance of 6, expressed as follows:

$$896 \quad P(q_t) = \begin{cases} \frac{1}{\delta} - \frac{|q_t - \bar{q}_t|}{\delta^2} & \text{if } |s| < 1 \\ 0 & \text{otherwise} \end{cases}$$

897 The cloud fraction b can be expressed as

$$\begin{aligned} 899 \quad b &= \int_{q_s}^{\infty} P(q_t) dq_t \\ 900 &= \int_{q_s}^{\infty} P(\delta s + \bar{q}_t) dq_t \\ 901 &= \int_{s_s}^{\infty} \left(\frac{1}{\delta} - \frac{|s|}{\delta} \right) \delta ds \\ 902 &= \int_{s_s}^{\infty} (1 - |s|) ds \\ 903 &= \begin{cases} \frac{1}{2}(1 - s_s)^2 & \text{if } s_s > 0 \\ 1 - \frac{1}{2}(1 + s_s)^2 & \text{if } s_s < 0 \end{cases} \end{aligned}$$

898 Cloud liquid water is then derived as

$$\begin{aligned} 904 \quad \bar{q}_l &= \int_{q_s}^{\infty} (q_t - q_s) P(q_t) dq_t \\ 905 &= \int_{q_s}^{\bar{q}_t + \delta} q_t P(\delta s + \bar{q}_t) dq_t \\ 906 &= \int_{s_s}^1 (\delta s - \delta s_s)(1 - |s|) ds \\ 907 &= \int_{s_s}^1 (\delta s)(1 - |s|) ds - \delta s_s \int_{s_s}^1 (1 - |s|) ds \\ 908 &= \int_{s_s}^1 \delta s(1 - |s|) ds - \delta s_s b \end{aligned}$$

909 Thus,

$$911 \quad \frac{\bar{q}_l}{\delta} = \int_{s_s}^1 s(1 - |s|) ds - s_s b$$

910 For $1 > s_s > 0$ (i.e., $\bar{q}_t < q_s$),

$$913 \quad \frac{\bar{q}_l}{\delta} = \int_{s_s}^1 s(1 - |s|) ds - s_s b = \frac{1}{6} - \frac{s_s^2}{6} + \frac{s_s^3}{6} - s_s b$$

912 For $-1 < s_s < 0$ (i.e., $\bar{q}_t > q_s$),

$$914 \quad \frac{\bar{q}_l}{\delta} = \int_{s_s}^1 s(1 - |s|) ds - s_s b$$

916
$$= \int_{s_s}^0 s(1+s)ds + \int_0^1 s(1-s)ds - s_s b$$

917
$$= -\frac{1}{6} - \frac{1}{6}(3s_s^2 - 2s_s^3) - s_s b$$

915 In summary,

919
$$\frac{\bar{q}_l}{\delta} = \begin{cases} \frac{1}{6} - \frac{s_s^2}{6} + \frac{s_s^3}{6} - s_s b & \text{if } \bar{q}_t < q_s \\ -\frac{1}{6} - \frac{1}{6}(3s_s^2 - 2s_s^3) - s_s b & \text{if } \bar{q}_t > q_s \end{cases}$$

918

920

921 References

922 Austin, R. T., Heymsfield, A. J., and Stephens, G. L.: Retrieval of ice cloud
923 microphysical parameters using the CloudSat millimeter-wave radar and
924 temperature, *J. Geophys. Res.*, 114, D00A23, doi:10.1029/2008JD010049, 2009.

925 Bogenschutz, P. A., Gettelman, A., Morrison, H., Larson, V. E., Craig, C., and Schanen,
926 D. S.: Higher-Order Turbulence Closure and Its Impact on Climate Simulations in
927 the Community Atmosphere Model, *J. Climate*, 26, 9655–9676, doi: 10.1175/JCLI-
928 D-13-00075.1, 2013.

929 Bogenschutz, P. A., Gettelman, A., Morrison, H., Larson, V. E., Schanen, D. P., Meyer,
930 N. R., and Craig, C.: Unified parameterization of the planetary boundary layer and
931 shallow convection with a higher-order turbulence closure in the Community
932 Atmosphere Model, *Geosci. Model Dev.*, 5, 1407–1423, 2012.

933 Bogenschutz, P. A., and Krueger, S. K.: A simplified pdf parameterization of subgrid-
934 scale clouds and turbulence for cloud-resolving models, *Journal of Advances in*
935 *Modeling Earth Systems*, 5 (2), 195–211, doi:10.1002/jame.20018, 2013.

936 Boucher, O., Randall, D., Artaxo, P., Bretherton, C., Feingold, G., Forster, P., Kerminen,
937 V.-M., Kondo, Y., Liao, H., Lohmann, U., Rasch, P., Satheesh, S.K., Sherwood, S.,
938 Stevens, B. and Zhang, X. Y.: Clouds and Aerosols. In: *Climate Change 2013: The*
939 *Physical Science Basis. Contribution of Working Group I to the Fifth Assessment*
940 *Report of the Intergovernmental Panel on Climate Change* [Stocker, T. F., D. Qin,
941 G.-K. Plattner, M. Tignor, S. K. Allen, J. Boschung, A. Nauels, Y. Xia, V. Bex and P.
942 M. Midgley (eds.)], Cambridge University Press, Cambridge, United Kingdom and
943 New York, NY, USA, 2013.

944 Bougeault, P.: Modeling the trade-wind cumulus boundary layer. Part II: A higher-order
945 one-dimensional model, *J. Atmos. Sci.*, 38, 2429–2439, 1981.

946 Chaboureau, J.-P., and Bechtold, P.: A Simple Cloud Parameterization Derived from
947 Cloud Resolving Model Data: Diagnostic and Prognostic Applications, *J. Atmos.*
948 *Sci.*, 59, 2362–2372, 2002.

949 Chen, W.-T., Woods, C. P., Li, J.-L. F., Waliser, D. E., Chern, J.-D., Tao, W.-K., Jiang,
950 J. H., and Tompkins, A. M.: Partitioning CloudSat ice water content for comparison
951 with upper-tropospheric ice in global atmospheric models, *J. Geophys. Res.*, 116,
952 D19206, doi:10.1029/2010JD015179, 2011.

953 Chosson, F., Vaillancourt, P. A., Milbrandt, J. A., Yau, M. K., and Zadra, A.: Adapting
954 Two-Moment Microphysics Schemes across Model Resolutions: Subgrid Cloud and
955 Precipitation Fraction and Microphysical Sub-Time Step, *J. Atmos. Sci.*, 71, 2635–
956 2653, doi: 10.1175/JAS-D-13-0367.1, 2014.

957 Dee, D. P., Uppala, S. M., Simmons, A. J., Berrisford, P., Poli, P., Kobayashi, S., Andrae,
958 U., Balmaseda, M. A., Balsamo, G., Bauer, P., Bechtold, P., Beljaars, A., van de Berg,
959 L., Bidlot, J., Bormann, N., Delsol, C., Dragani, R., Fuentes, M., Geer, A. J.,
960 Haimberger, L., Healy, S. B., Hersbach, H., Hólm, E. V., Isak-sen, L., Kallberg, P.,
961 Köhler, M., Matricardi, M., McNally, A.P., Monge-Sanz, B. M., Morcrette, J.-J.,
962 Park, B. K., Peubey, C., de Rosnay, P., Tavolato, C., Thépaut, J.-N., and Vitart, F.:
963 The ERA-Interim reanalysis: configuration and performance of the data assimilation
964 system, *Q. J. Roy. Meteorol. Soc.*, 137, 553–597, doi:10.1002/qj.828, 2011.

965 Donner, et al.: The Dynamical Core, Physical Parameterizations, and Basic Simulation
966 Characteristics of the Atmospheric Component AM3 of the GFDL Global Coupled
967 Model CM3, *J. Clim.*, 24, 3484–3519, doi: 10.1175/2011JCLI3955.1, 2011.

968 Firl, G. J.: A Study of Low Cloud Climate Feedbacks Using a Generalized Higher-
969 Order Closure Subgrid Model, PhD Dissertation, Department of Atmospheric
970 Science, Colorado State University, 253pp, 2013.

971 Firl, G. J., and Randall, D. A.: Fitting and Analyzing LES Using Multiple Trivariate
972 Gaussians, *J. Atmos. Sci.*, 72, 1094–1116, 2015.

973 Franklin, C. N., Jakob, C., Dix, M., Protat, A., and Roff, G.: Assessing the performance
974 of a prognostic and a diagnostic cloud scheme using single column model
975 simulations of TWP-ICE, *Q. J. R. Meteorol. Soc.*, 138, 734–754. doi:10.1002/qj.954,
976 2012.

977 Golaz, J.-C., Horowitz, L. W., and Levy, II H.: Cloud tuning in a coupled climate model:
978 impact on 20th century warming, *Geophys. Res. Lett.*, 40, 2246–2251,
979 doi:10.1002/grl.50232, 2013.

980 Golaz, J., Larson, V., and Cotton, W.: A PDF-based model for boundary layer clouds:
981 Part 1. Method and model description, *J. Atmos. Sci.*, 59 (24), 3540–3551, 2002.

982 Hogan, R. J., O’Connor, E. J., and Illingworth, A. J.: Verification of cloud fraction
983 forecasts, *Q. J. R. Meteorol. Soc.*, 135, 1494–1511, 2009.

984 Hourdin, F., Mauritsen, T., Gettelman, A., Golaz, J.-C., Balaji, V., Duan, Q., Folini, D.,
985 Ji, D., Klocke, D., Qian, Y., Rauser, F., Rio, C., Tomassini, L., Watanabe, M., and
986 Williamson, D.: The art and science of climate model tuning, *Bulletin of the*

987 American Meteorological Society, published online, doi: 10.1175/BAMS-D-15-
988 00135.1, 2016.

989 Jakob, C., and Klein, S. A.: A parameterization of the effects of cloud and precipitation
990 overlap for use in general circulation models, *Quart. J. Roy. Meteor. Soc.*, 126, 2525–
991 2544, doi:10.1002/qj.49712656809, 2000.

992 Kay, J. E., Hillman, B., Klein, S., Zhang, Y., Medeiros, B., Gettelman, G., Pincus, R.,
993 Eaton, B., Boyle, J., Marchand, R. and Ackerman, T.: Exposing global cloud biases
994 in the Community Atmosphere Model (CAM) using satellite observations and their
995 corresponding instrument simulators, *J. Climate*, 25, 5190–5207. doi:
996 <http://dx.doi.org/10.1175/JCLI-D-11-00469.1>, 2012.

997 Larson, V. E., Golaz, J.-C., and Cotton, W. R.: Small-scale and mesoscale variability in
998 cloudy boundary layers: Joint probability density functions, *J. Atmos. Sci.*, 59,
999 3519–3539, 2002.

1000 Lee, W.-L., Wang, Y.-C., Shiu, C.-J., Tsai, I., Tu, C.-Y., Lan, Y.-Y., Chen, J.-P., Pan, H.-
1001 L., and Hsu, H.-H.: Taiwan Earth System Model Version 1: Description and
1002 Evaluation of Mean State, *Geosci. Model Dev. Discuss.*,
1003 <https://doi.org/10.5194/gmd-2019-377>, in review, 2020.

1004 Li, J.-L. F., Waliser, D. E., Chen, W.-T., Guan, B., Kubar, T. L., Stephens, G. L., Ma,
1005 H.-Y., Min, D., Donner, L. J., Seman, C. J., and Horowitz, L. W.: An observationally-
1006 based evaluation of cloud ice water in CMIP3 and CMIP5 GCMs and contemporary
1007 reanalyses using contemporary satellite data, *J. Geophys. Res.*,
1008 doi:10.1029/2012JD017640, 2012.

1009 Lin, Y.: Humidity variability revealed by a sounding array and its implications for cloud
1010 representation in GCMs, *J. Geophys. Res. Atmos.*, 119, 10,499–10,514,
1011 doi:10.1002/2014JD021837, 2014.

1012 Marchand, R., Mace, G. G., Ackerman, T., and Stephens, G.: Hydrometeor Detection
1013 Using Cloudsat—An Earth-Orbiting 94-GHz Cloud Radar, *J. Atmos. Oceanic*
1014 *Technol.*, 25, 519–533, 2008.

1015 Mauritsen, T., et al.: Tuning the climate of a global model, *J. Adv. Model. Earth Syst.*,
1016 4, M00A01, doi:10.1029/2012MS000154, 2012.

1017 May, P. T., Mather, J. H., Vaughan, G., Jakob, C., McFarquhar, G. M., Bower, K. N.,
1018 and Mace, G. G.: The Tropical Warm Pool International Cloud Experiment, *Bull.*
1019 *Amer. Meteor. Soc.*, 89, 629–645, 2008.

1020 McCoy, D. T., Tan, I., Hartmann, D. L., Zelinka, M. D., and Storelvmo, T.: On the
1021 relationships among cloud cover, mixed-phase partitioning, and planetary albedo in
1022 GCMs, *J. Adv. Model. Earth Syst.*, 8, 650–668, doi:10.1002/2015MS000589, 2016.

1023 Molod, A.: Constraints on the Profiles of Total Water PDF in AGCMs from AIRS and
1024 a High-Resolution Model, *J. Climate*, 25, 8341–8352, 2012.

1025 Neale, R. B. et al.: Description of the NCAR Community Atmosphere Model (CAM
1026 5.0), NCAR technical note (NCAR/TN-486+STR), National Center For
1027 Atmospheric Research Boulder, Colorado, USA, 2010.

1028 Neale R. B. et al.: The Mean Climate of the Community Atmosphere Model (CAM4)
1029 in Forced SST and Fully Coupled Experiments, *J. Climate*, 26, 5150–5168, doi:
1030 10.1175/JCLI-D-12-00236.1, 2013.

1031 Park, R.-S., Chae, J.-H., and Hong, S.-Y.: A Revised Prognostic Cloud Fraction Scheme
1032 in a Global Forecasting System, *Mon. Wea. Rev.*, 144, 1219–1229, doi:
1033 10.1175/MWR-D-15-0273.1, 2016.

1034 Park, S., Bretherton, C. S., and Rasch, P. J.: Integrating Cloud Processes in the
1035 Community Atmosphere Model, Version 5, *J. Climate*, 27, 6821–6856, 2014.

1036 Park, S.: A unified convection scheme (UNICON). Part I: Formulation, *J. Atmos. Sci.*,
1037 71, 3902–3930, 2014a.

1038 Park, S.: A unified convection scheme (UNICON). Part II: Simulation, *J. Atmos. Sci.*,
1039 71, 3931–3973, 2014b.

1040 Qian, Y., Long, C. Wang, N., H., Comstock, J. M., McFarlane, S. A., and Xie, S.:
1041 Evaluation of cloud fraction and its radiative effect simulated by IPCC AR4 global
1042 models against ARM surface observations, *Atmos. Chem. Phys.*, 12, 1785–1810,
1043 doi:10.5194/acp-12-1785-2012, 2012.

1044 Quaas, J.: Evaluating the “critical relative humidity” as a measure of subgrid-scale
1045 variability of humidity in general circulation model cloud cover parameterizations
1046 using satellite data, *J. Geophys. Res.*, 117, D09208, doi:10.1029/2012JD017495,
1047 2012.

1048 Rasch, P. J., and Kristjansson, J. E.: A comparison of the CCM3 model climate using
1049 diagnosed and predicted condensate parameterizations, *J. Climate*, 11, 1587–1614,
1050 doi:10.1175/1520-0442(1998)011,1587:ACOTCM.2.0.CO;2, 1998.

1051 Roeckner, E., et al.: The atmospheric general circulation model ECHAM-4: Model
1052 description and simulation of present-day climate, Rep. 218, 90 pp., Max Planck
1053 Institute for Meteorology, Hamburg, Germany, 1996.

1054 Salzmann, M., Ming, Y., Golaz, J. C., Ginoux, P. Morrison, A., Gettelman, H., A.,
1055 Krämer, M., and Donner, L. J.: Two-moment bulk stratiform cloud microphysics in
1056 the GFDL AM3 GCM: Description, evaluation, and sensitivity tests, *Atmos. Chem.*
1057 *Phys.*, 10, 8037–8064, doi:10.5194/acp-10-8037-2010, 2010.

1058 Schmidt, G. A., et al.: Configuration and assessment of the GISS ModelE2
1059 contributions to the CMIP5 archive, *J. Adv. Model. Earth Syst.*, 6, 141–184,
1060 doi:10.1002/2013MS000265, 2014.

1061 Slingo, J. M.: The development and verification of a cloud prediction scheme for the
1062 ECMWF model, *Quart. J. Roy. Meteor. Soc.*, 113, 899–927,

1063 doi:10.1002/qj.49711347710, 1987.

1064 Smith, R.: A scheme for predicting layer clouds and their water content in a general
 1065 circulation model, *Quart. J. Roy. Meteor. Soc.*, 116, 435–460,
 1066 doi:10.1002/qj.49711649210, 1990.

1067 Sommeria, G., and Deardorff, J. W.: Subgrid-scale condensation in models of
 1068 nonprecipitating clouds, *J. Atmos. Sci.*, 34, 344–355, 1977.

1069 Sotiropoulou, G., Sedlar, J., Forbes, R., and Tjernstrom, M.: Summer Arctic clouds in
 1070 the ECMWF forecast model: an evaluation of cloud parameterization schemes, *Q. J.
 1071 R. Meteorol. Soc.*, doi:10.1002/qj.2658, (2015).

1072 Storer, R. L., Griffin, B. Hoft, M., J., Weber, J. K., Raut, E., Larson, V. E., Wang, M.,
 1073 and Rasch, P. J.: Parameterizing deep convection using the assumed probability
 1074 density function method, *Geosci. Model. Dev.*, 8 (1), 1–19, doi:10.5194/gmd-8-1-
 1075 2015, 2015.

1076 Su, H., et al.: Diagnosis of regime-dependent cloud simulation errors in CMIP5 models
 1077 using “A-Train” satellite observations and reanalysis data, *J. Geophys. Res. Atmos.*,
 1078 118, 2762–2780, doi:10.1029/2012JD018575, 2013.

1079 Sundqvist, H.: Parameterization of condensation and associated clouds in models for
 1080 weather prediction and general circulation simulation, *Physically Based Modeling
 1081 and Simulation of Climate and Climatic Change*, M. E. Schlesinger, Ed., Kluwer
 1082 Academic, 433–461, 1988.

1083 Sundqvist, H., Berge, E., and Kristjansson, J. E.: Condensation and cloud
 1084 parameterization studies with a mesoscale numerical weather prediction model, *Mon.
 1085 Wea. Rev.*, 117, 1641–1657, doi:10.1175/15200493(1989)117, 1989.

1086 Tiedtke, M.: Representation of clouds in large-scale models, *Mon. Wea. Rev.*, 121,
 1087 3040–3061, doi:10.1175/1520-0493(1993)121,3040:ROCILS.2.0.CO;2, 1993.

1088 Tompkins, A. M.: A prognostic parameterization for the subgrid-scale variability of
 1089 water vapor and clouds in large-scale models and its use to diagnose cloud cover, *J.
 1090 Atmos. Sci.*, 59, 1917–1942, doi:10.1175/1520-0469(2002)059, 2002.

1091 Tompkins, A. M.: The parametrization of cloud cover, *ECMWF Moist Processes
 1092 Lecture Note Series*, p. available at <http://www.ecmwf.int/newsevents/training/>,
 1093 2005.

1094 Tompkins, A. M., Gierens, K., and Rädcl, G.: Ice supersaturation in the ECMWF
 1095 integrated forecast system, *Quart. J. Roy. Meteor. Soc.*, 133, 53–63,
 1096 doi:10.1002/qj.14, 2007.

1097 Wilson, D. R., Bushell, A. C., Kerr-Munslow, A. M., Price, J. D., Morcrette, C. J.: PC2:
 1098 A prognostic cloud fraction and condensation scheme. I: Scheme description, *Q. J.
 1099 R. Meteorol. Soc.* 134: doi: 10.1002/qj.333, 2008a.

1100 Wilson, D. R., Bushell, A. C., Kerr-Munslow, A. M., Price, J. D., Morcrette, C. J.,

1101 Bodas-Salcedo, A.: PC2: A prognostic cloud fraction and condensation scheme. II:
1102 Climate model simulations, *Q. J. R. Meteorol. Soc.* 134: 2109–2125, doi:
1103 10.1002/qj.332, 2008b.

1104 Xie, S., Hume, T., Jakob, C., Klein, S., McCoy, R., and Zhang, M.: Observed large-
1105 scale structures and diabatic heating and drying profiles during TWP-ICE, *J. Climate*,
1106 23, 57–79, 2010.

1107 Xu, K. M., and Randall, D. A.: A semiempirical cloudiness parameterization for use in
1108 climate models, *J. Atmos. Sci.*, 53, 3084–3102, doi:10.1175/1520-
1109 0469(1996)053<3084:ASCPFU.2.0.CO;2, 1996.

1110 Zhang, M., Lin, W., Bretherton, C., Hack, J., and Rasch, P. J.: A modified formulation
1111 of fractional stratiform condensation rate in the NCAR Community Atmospheric
1112 Model (CAM2), *J. Geophys. Res.*, 108(D1), 4035, doi:10.1029/2002JD002523,
1113 2003.

1114
1115
1116

1117

1118 Code availability

1119 The codes of the GTS scheme used in this study can be obtained from the following
1120 website:

1121 <https://doi.org/10.5281/zenodo.3626654>

1122

1123

1124 Author contributions. HHH is the initiator and primary investigator of the TaiESM
1125 project. CJS developed code and wrote the majority of the paper. YCW also developed
1126 code and wrote part of the paper. WTC helped process CloudSat/CALIPSO satellite
1127 data. HLP and RS helped develop the theoretical basis of the GTS scheme. YHC helped
1128 with the off-line calculations. CAC helped with most of the visualizations.

1129

1130

1131 Competing interests. The authors declare that they have no conflict of interest.

1132

1133

1134

1135

1136

1137

1138 Acknowledgements

1139 We would like to dedicate this paper to Dr. Chia Chou in appreciation for his
1140 encouragement. The work is supported in part by the Ministry of Science and
1141 Technology (MOST), Taiwan (R.O.C.) under the projects MOST 100-2119-M-001-
1142 029-MY5 and 105-2119-M-002-028-MY3. This work is also part of the Consortium
1143 for Climate Change Study (CCliCs) – Laboratory for Climate Change Research.
1144 CloudSat data is available through Austin *et al.* [2009]. Other observations, satellite
1145 retrievals, and reanalysis data used in the paper were obtained from the AMWG
1146 diagnostic package provided by CESM, NCAR. Detailed information regarding those
1147 observational data are available at
1148 <http://www.cgd.ucar.edu/amp/amwg/diagnostics/plotType.html>. We would like to
1149 thank Anthony Abram (www.uni-edit.net) for editing and proofreading this manuscript.

1150

1151

1152

Table 1. Root-mean-square errors (RMSE) for comparisons of latitude–height cross-sections of CF among the three macrophysical schemes (Park: default scheme; T_pdf: triangular PDF in the GTS scheme; U_pdf: uniform PDF in the GTS scheme) and observational data from CloudSat/CALIPSO (Figure 6). Comparisons are made of the means for five latitudinal ranges and three periods (JJA: June, July, August; DJF: December, January, February). The smallest RMSE value of the three schemes in each case is bold and underlined.

	Global			60°N~60°S			30°N~30°S			30°N~90°N			30°S~90°S		
	Park	T_pdf	U_pdf	Park	T_pdf	U_pdf	Park	T_pdf	U_pdf	Park	T_pdf	U_pdf	Park	T_pdf	U_pdf
Annual	7.15	8.27	<u>6.75</u>	5.25	<u>4.53</u>	4.85	5.84	5.37	<u>5.05</u>	8.78	10.40	<u>8.52</u>	6.46	8.29	<u>6.18</u>
JJA	<u>7.40</u>	11.30	9.50	6.27	5.64	<u>5.61</u>	6.03	5.96	<u>5.56</u>	<u>8.91</u>	10.60	9.13	<u>6.93</u>	15.50	12.70
DJF	9.04	9.37	<u>6.99</u>	5.62	<u>5.24</u>	5.38	6.29	5.53	<u>5.36</u>	12.80	13.00	<u>10.00</u>	6.33	7.85	<u>3.82</u>

Table 2. RMSEs for comparisons between CF at nine pressure levels, as simulated by the three macrophysical schemes (Park, T_pdf, U_pdf) and observational data from CloudSat/CALIPSO (Figure 7). The comparisons are made for three periods (JJA: June, July, August; DJF: December, January, February). The smallest RMSE value of the three schemes in each case is bold and underlined.

	Annual			JJA			DJF		
	Park	T_pdf	U_pdf	Park	T_pdf	U_pdf	Park	T_pdf	U_pdf
100 mb	6.07	5.40	<u>4.71</u>	<u>4.85</u>	12.70	10.10	7.88	<u>3.94</u>	4.20
125 mb	<u>4.70</u>	5.56	4.80	<u>6.13</u>	12.60	10.10	5.96	<u>4.56</u>	4.81
200 mb	7.23	8.34	<u>6.78</u>	<u>9.80</u>	14.90	11.90	8.64	6.57	<u>6.46</u>
300 mb	10.80	9.63	<u>7.98</u>	11.60	12.90	<u>10.80</u>	12.40	11.70	<u>9.06</u>
400 mb	11.80	10.50	<u>6.93</u>	12.40	10.50	<u>9.55</u>	12.70	13.90	<u>8.06</u>
500 mb	11.00	11.50	<u>7.65</u>	11.90	10.60	<u>9.28</u>	11.70	13.40	<u>8.50</u>
700 mb	8.64	9.47	<u>8.19</u>	9.63	10.80	<u>9.46</u>	10.70	11.10	<u>9.41</u>
850 mb	14.30	14.20	<u>12.00</u>	14.80	15.40	<u>12.80</u>	16.10	15.30	<u>13.20</u>
900 mb	12.50	15.10	<u>12.30</u>	<u>13.30</u>	16.60	13.60	15.10	16.40	<u>12.90</u>

Table 3. (a) RMSE and (b) R values for comparisons between CF and CWC simulated by the three macrophysical schemes (Park, T_pdf, and U_pdf) and plotted against vertical velocity at 500 mb (ω_{500}) or averaged RH for 300–1000 mb (RH300–1000, obtained from the ERA-Interim reanalysis) and observational data from CloudSat/CALIPSO (Figures 9 and 10). The comparisons are made for three latitudinal ranges. The smallest RMSE or largest R value of the three schemes in each case is bolded and underlined.

(a)

RMSE		Global			60°N~60°S			30°N~30°S		
		Park	T_pdf	U_pdf	Park	T_pdf	U_pdf	Park	T_pdf	U_pdf
OMEGA@500 mb	CWC	11.10	10.90	<u>9.83</u>	11.40	11.20	<u>10.10</u>	14.10	13.80	<u>12.50</u>
	CF	7.65	7.26	<u>6.13</u>	7.55	7.23	<u>6.24</u>	8.13	8.07	<u>7.21</u>
RH@300-1000 mb	CWC	<u>8.73</u>	9.69	11.60	13.50	15.10	<u>11.80</u>	19.10	18.00	<u>12.00</u>
	CF	17.90	18.30	<u>13.90</u>	15.40	17.30	<u>12.70</u>	18.80	18.30	<u>12.90</u>

(b)

R		Global			60°N~60°S			30°N~30°S		
		Park	T_pdf	U_pdf	Park	T_pdf	U_pdf	Park	T_pdf	U_pdf
OMEGA@500 mb	CWC	0.73	0.77	<u>0.80</u>	0.74	0.77	<u>0.80</u>	0.60	0.66	<u>0.74</u>
	CF	0.84	0.85	<u>0.89</u>	0.85	0.85	<u>0.88</u>	0.83	0.82	<u>0.84</u>
RH@300-1000 mb	CWC	<u>0.64</u>	0.54	0.45	0.44	0.34	<u>0.62</u>	0.22	0.25	<u>0.55</u>
	CF	0.31	0.40	<u>0.59</u>	0.51	0.46	<u>0.68</u>	0.45	0.45	<u>0.66</u>

Table 4. Global annual means (Mean) and RMSE values for comparisons with the observed values (Obs) for a selection of climatic parameters simulated by the three cloud macrophysical schemes (Park, T_pdf, and U_pdf). The smallest RMSE value or closest global mean of the three schemes in each case is bolded and underlined.

Parameters	Obs	Mean (Park)	Mean (T_pdf)	Mean (U_pdf)	RMSE (Park)	RMSE (T_pdf)	RMSE (U_pdf)
RESTOA_CERES-EBAF	0.81	4.18	3.25	<u>-1.06</u>	12.39	<u>10.43</u>	11.11
FLUT_CERES-EBAF	239.67	234.97	237.88	<u>238.14</u>	8.78	6.73	<u>6.50</u>
FLUTC_CERES-EBAF	265.73	259.06	259.65	<u>260.45</u>	7.55	7.12	<u>6.48</u>
FSNTOA_CERES-EBAF	240.48	<u>239.15</u>	241.14	237.08	13.97	<u>11.64</u>	12.79
FSNTOAC_CERES-EBAF	287.62	<u>291.26</u>	291.31	291.70	<u>7.08</u>	7.09	7.58
LWCF_CERES-EBAF	26.06	<u>24.10</u>	21.77	22.31	6.78	6.77	<u>6.21</u>
SWCF_CERES-EBAF	-47.15	-52.11	<u>-50.18</u>	-54.61	15.98	<u>12.90</u>	15.43
PRECT_GPCP	2.67	<u>2.97</u>	3.04	3.14	<u>1.09</u>	1.10	1.15
PREH2O ERAI	24.25	25.64	24.90	<u>24.45</u>	2.56	2.05	<u>2.03</u>
CLDTOT_Cloudsat+CALIPSO	66.82	<u>64.11</u>	70.77	70.09	9.87	11.38	<u>9.76</u>
CLDHGH_Cloudsat+CALIPSO	40.33	38.17	44.79	<u>40.22</u>	9.37	9.28	<u>8.17</u>
CLDMED_Cloudsat+CALIPSO	32.16	27.22	30.41	<u>31.26</u>	8.03	6.95	<u>6.28</u>
CLDLOW_Cloudsat+CALIPSO	43.01	<u>43.63</u>	43.67	46.19	<u>12.78</u>	18.06	16.17
CLDTOT_CALIPSO GOCCP	67.25	56.43	55.45	<u>61.72</u>	14.38	15.37	<u>10.28</u>
CLDHGH_CALIPSO GOCCP	32.04	<u>25.57</u>	22.48	24.46	<u>9.04</u>	11.30	10.16
CLDMED_CALIPSO GOCCP	18.09	11.21	14.55	<u>18.19</u>	8.35	6.34	<u>6.02</u>
CLDLOW_CALIPSO GOCCP	37.95	33.24	33.16	<u>38.41</u>	10.63	11.33	<u>9.98</u>
TGCLDLWP(ocean)	79.87	42.55	40.68	<u>48.74</u>	40.92	42.37	<u>35.16</u>
U_200_MERRA	15.45	16.18	15.87	<u>15.66</u>	2.52	2.11	<u>1.94</u>
T_200 ERAI	218.82	215.58	215.76	<u>216.84</u>	4.03	3.37	<u>2.13</u>

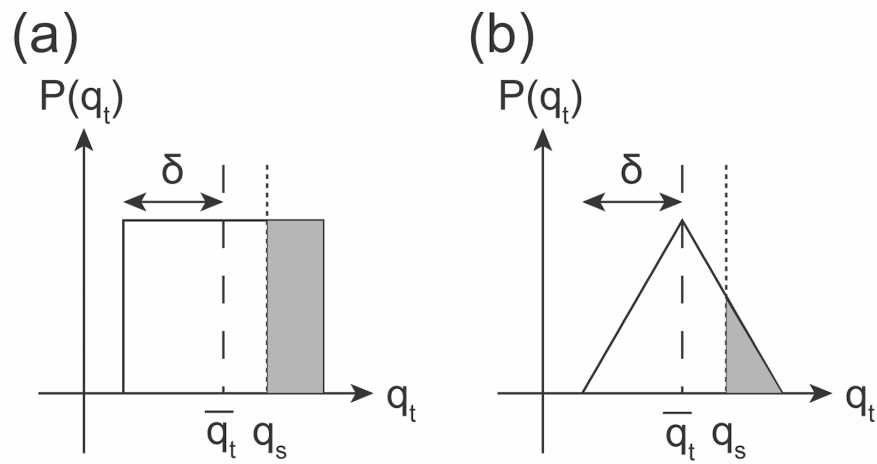


Figure 1. Illustration of sub-grid PDF of total water substance q_t with (a) uniform distribution and (b) triangular distribution. The shaded part shows the saturated cloud fraction, δ represents the width of the PDF, \bar{q}_t denotes the grid-mean value of total water substance, and q_s represents the saturation mixing ratio as the temperature is assumed to be uniform within the grid. Please note that uniform temperature assumption is used for the GTS cloud macrophysics.

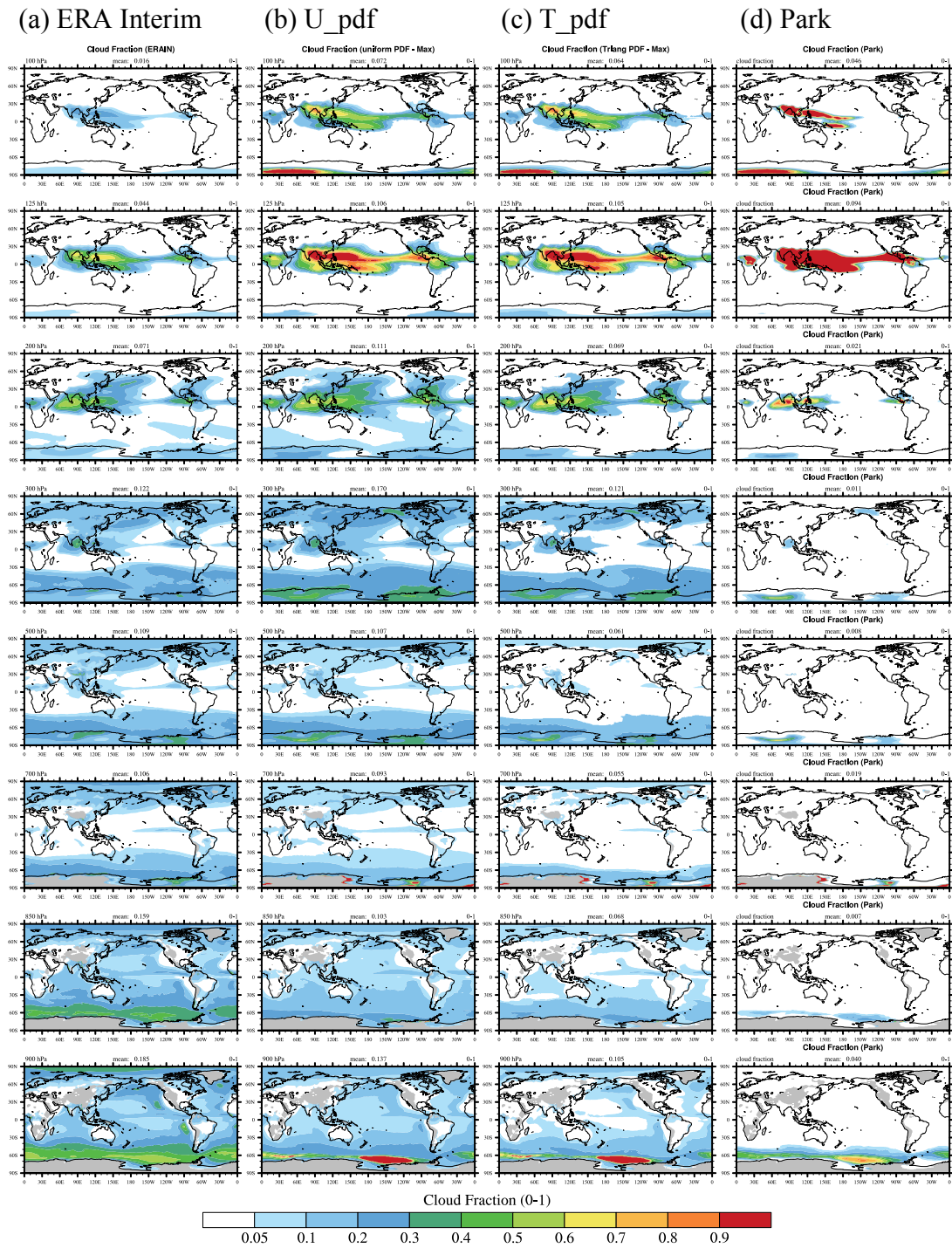


Figure 2. Mean cloud fraction in July (a) from the ERA-Interim reanalysis dataset and (b, c, d) diagnosed from cloud fraction schemes, with temperature, moisture, and condensates from the ERA-Interim reanalysis provided. From left to right, these schemes are the (b) U_pdf, (c) T_pdf, and (d) Park macrophysics schemes. Cloud distributions from 100 to 900 hPa are plotted from top to bottom.

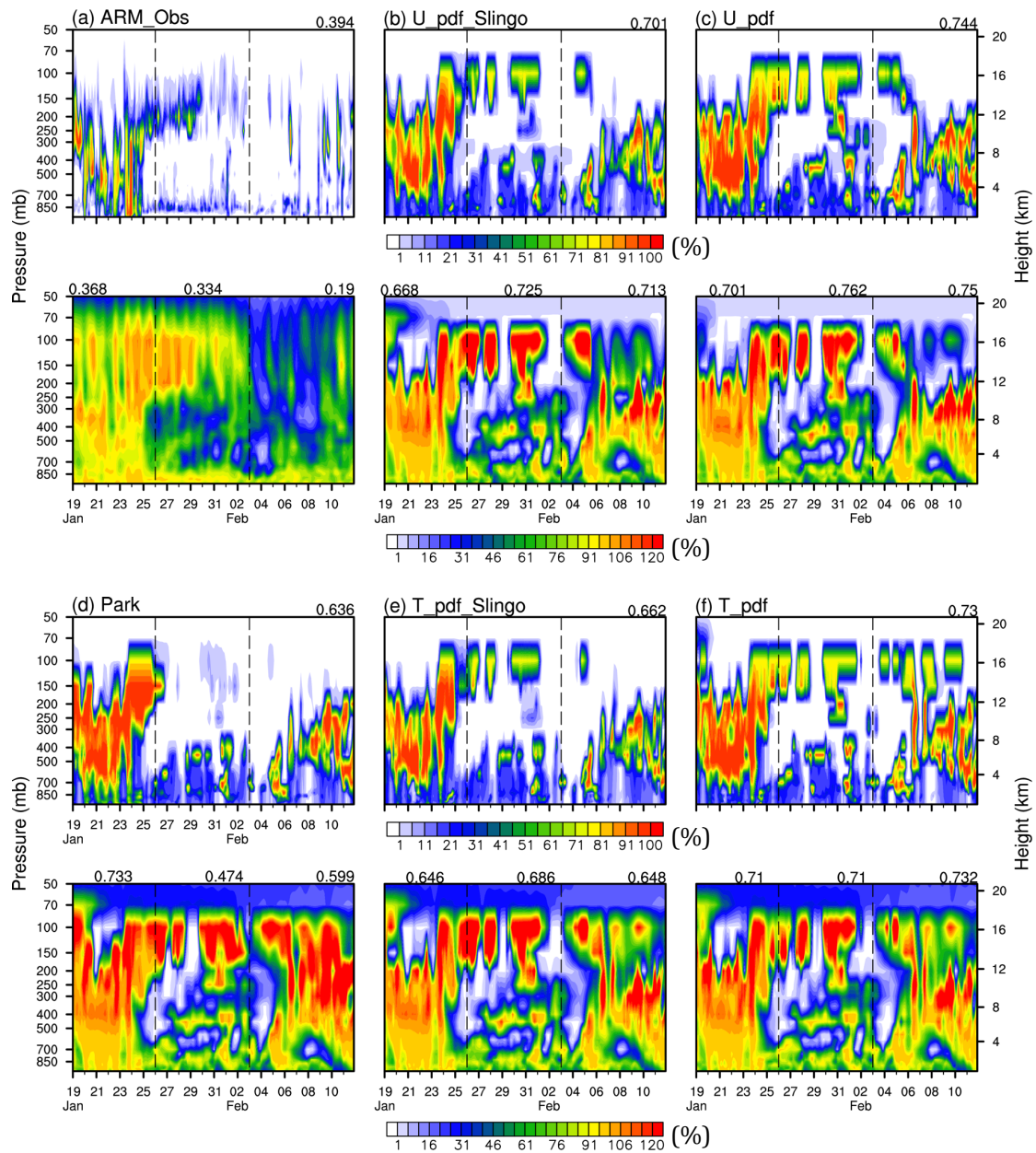


Figure 3. Pressure–time cross-sections of cloud fraction (upper panel) and relative humidity (lower panel) observed by (a) Xie *et al.* [2010] and simulated by SCAM with the (b) U_pdf with Slingo ice CF scheme, (c) U_pdf, (d) Park of CAM5.3, (e) T_pdf with Slingo ice CF scheme, and (f) T_pdf cloud macrophysics schemes.

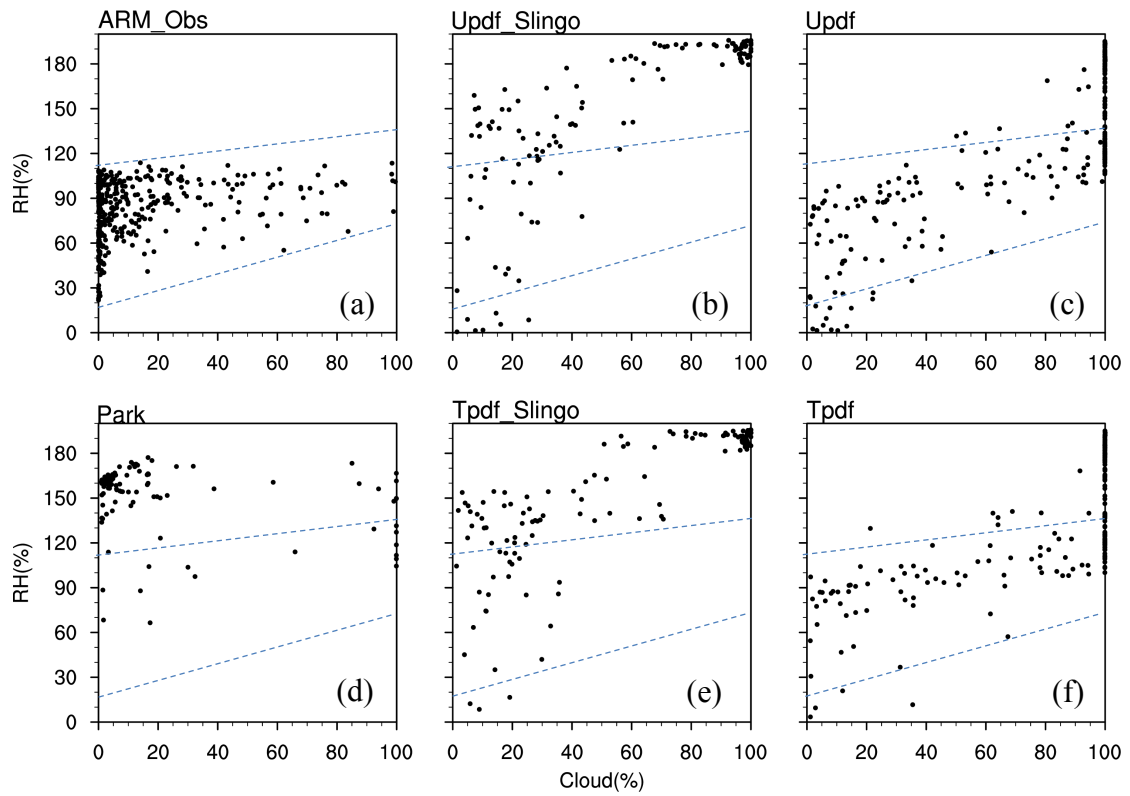


Figure 4. Scatter plots of high-level (50–300 hPa) relative humidities and cloud fractions during the suppressed monsoon period of the TWP-ICE field campaign (26 January to 3 February, 2006) observed by (a) Xie *et al.* [2010] and simulated by SCAM with the (b) U_pdf with Slingo ice CF scheme, (c) U_pdf, (d) Park of CAM5.3, (e) T_pdf with Slingo ice CF scheme, and (f) T_pdf cloud macrophysics schemes. Two dashed blue lines are also shown in the figure to enclose the observational RH-CF distributions.

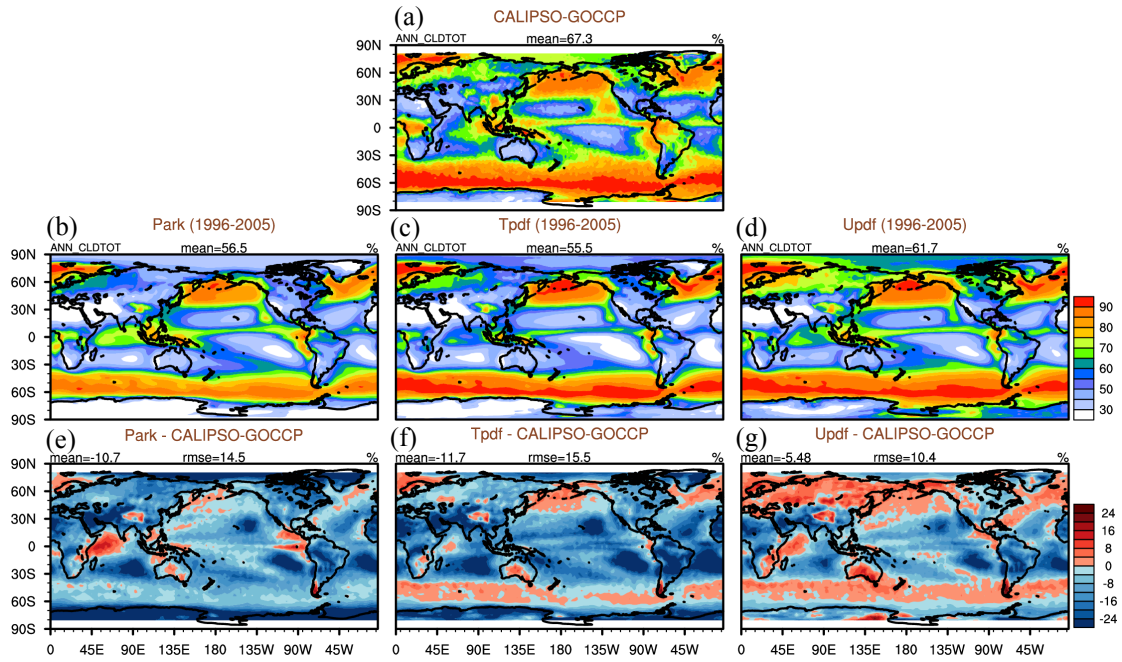


Figure 5. Total cloud fraction (CF) from (a) CALIPSO-GOCCP and simulated by the three schemes: (b) the default Park, (c) T_pdf, and (d) U_pdf, using the COSP satellite simulator of the NCAR CESM model. Differences between the simulated and observed total CFs derived from (e) the default Park, (f) T_pdf, and (g) U_pdf schemes.

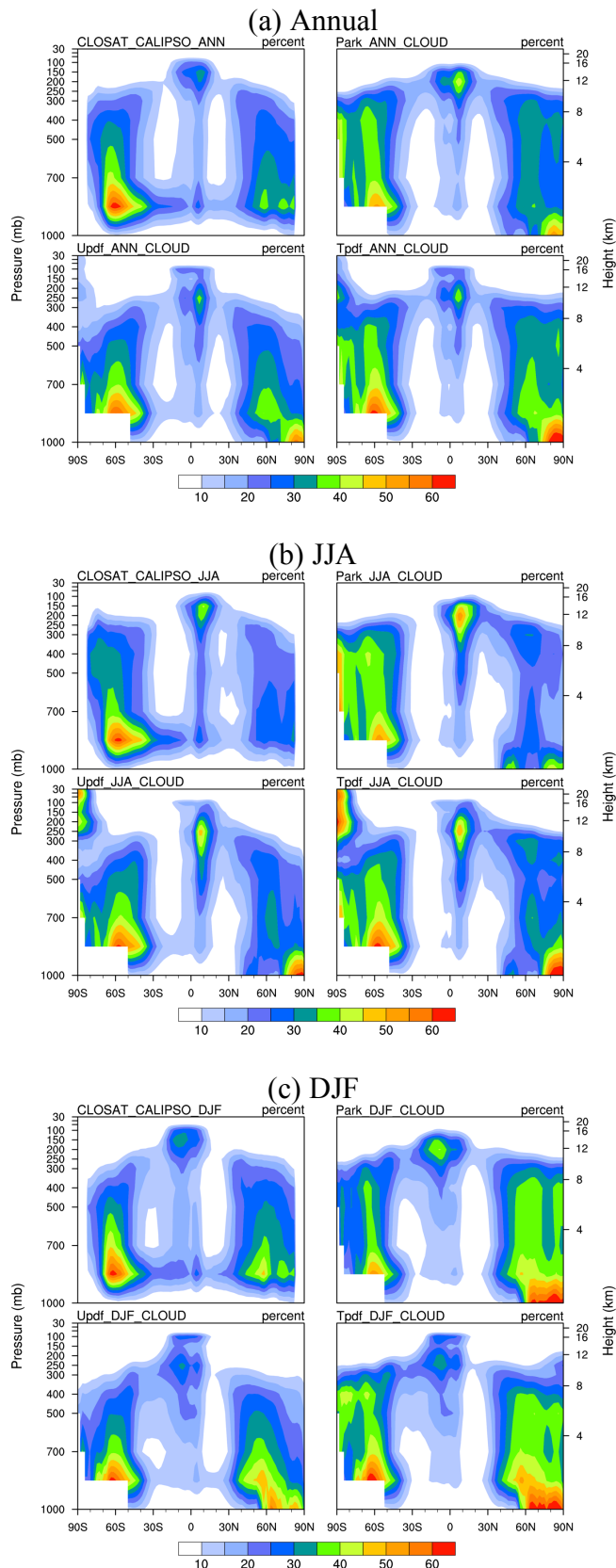


Figure 6. Latitude–height cross-sections of (a) annual, (b) June–July–August (JJA), and (c) December–January–February (DJF) mean CFs from CloudSat/CALIPSO data (upper left) and the the Park (upper right), U_pdf (lower left), and T_pdf (lower right) schemes.

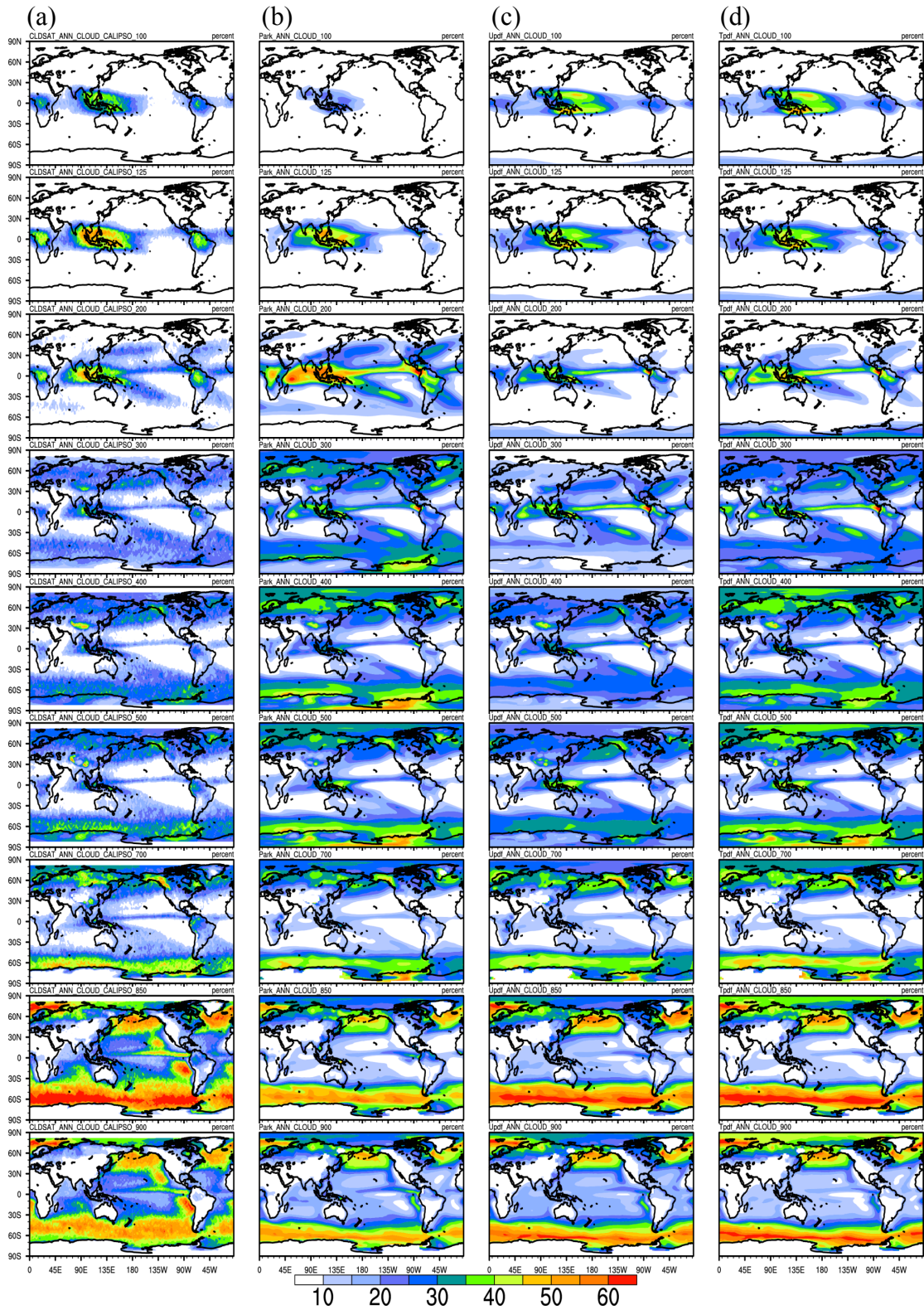


Figure 7. CFs at nine pressure levels (one pressure level per row; top to bottom: 100, 125, 200, 300, 400, 500, 700, 850, and 900 mb) from (a) CloudSat/CALIPSO observational data and simulated by (b) the default Park, (c) U_pdf, and (d) T_pdf schemes.

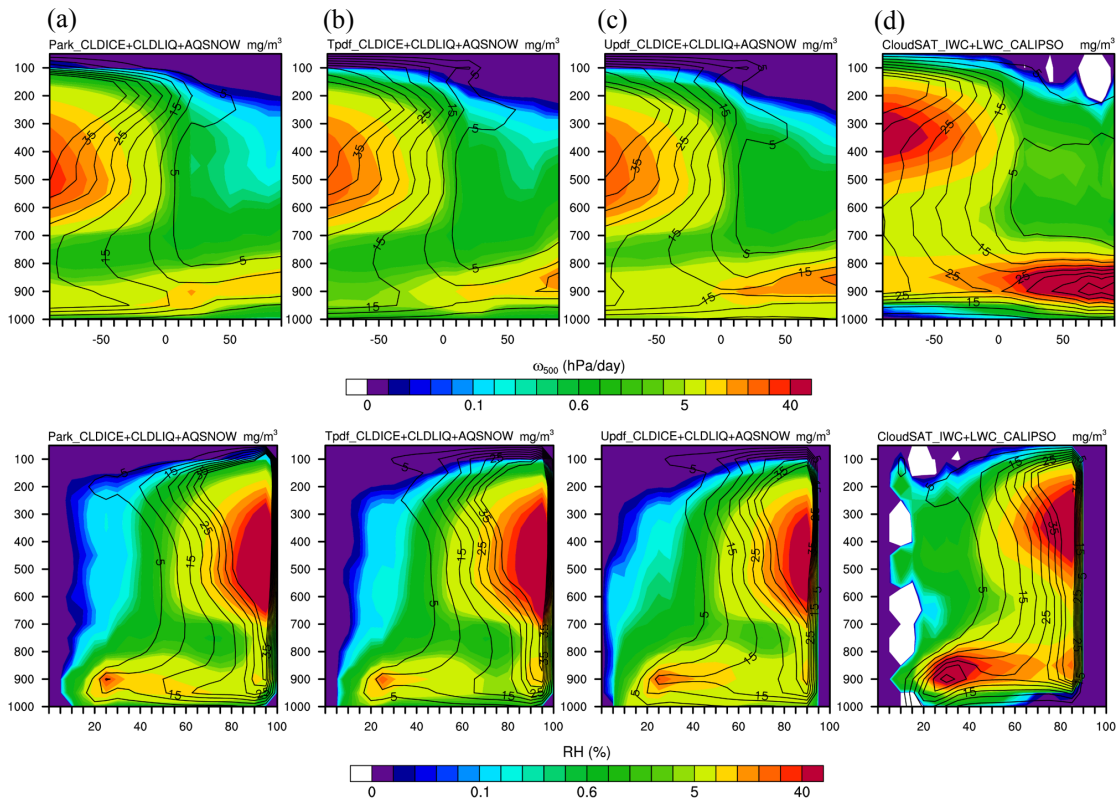


Figure 8. Vertical distribution of CF (contour lines) and CWC (colors) as functions of two large-scale parameters: vertical velocity at 500 mb (ω_{500} , upper four panels) and relative humidity averaged between 300 and 1000 mb (RH_{300–1000}, lower four panels) for the latitudinal range 30° N–30° S. Columns present simulations by the (a) Park, (b) T_pdf, and (c) U_pdf schemes, and (d) observational data from CloudSat/CALIPSO.

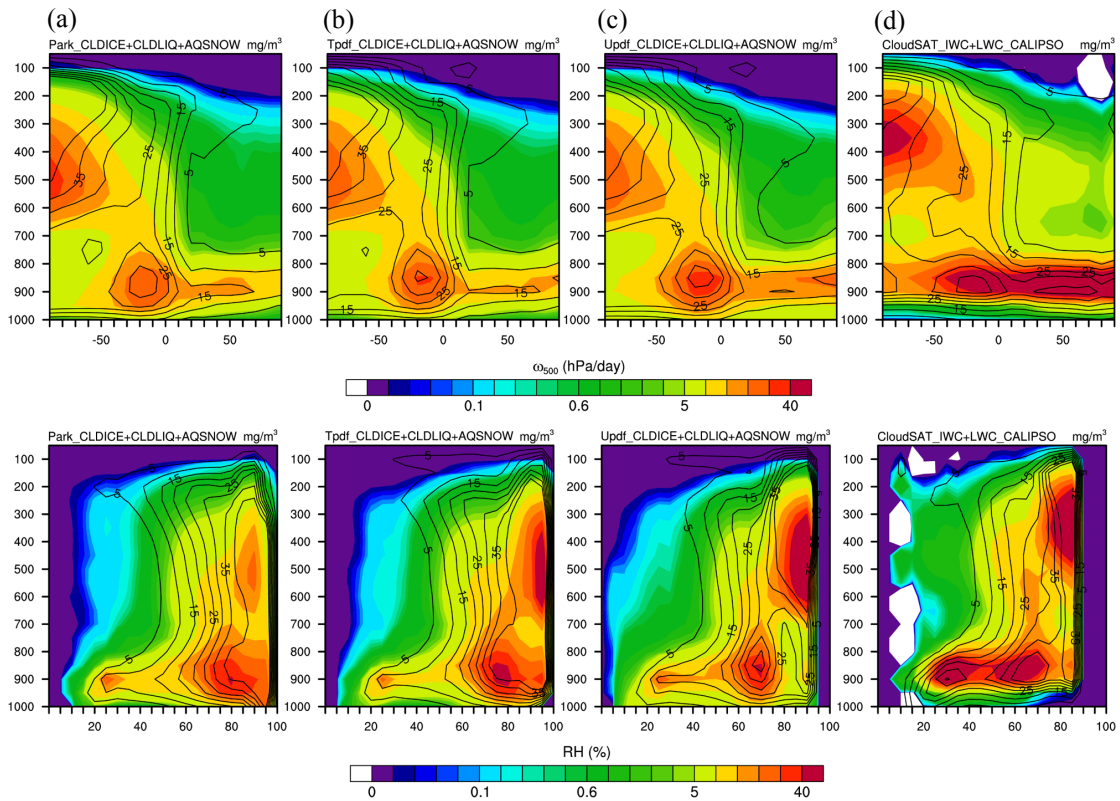


Figure 9. Vertical distribution of CF (contour lines) and CWC (colors) as functions of two large-scale parameters: ω_{500} (upper four panels) and RH_{300–1000} (lower four panels) for the latitudinal range 60° N–60° S. Columns present simulations by the (a) Park, (b) T_pdf, and (c) U_pdf, and (d) observational data from CloudSat/CALIPSO.

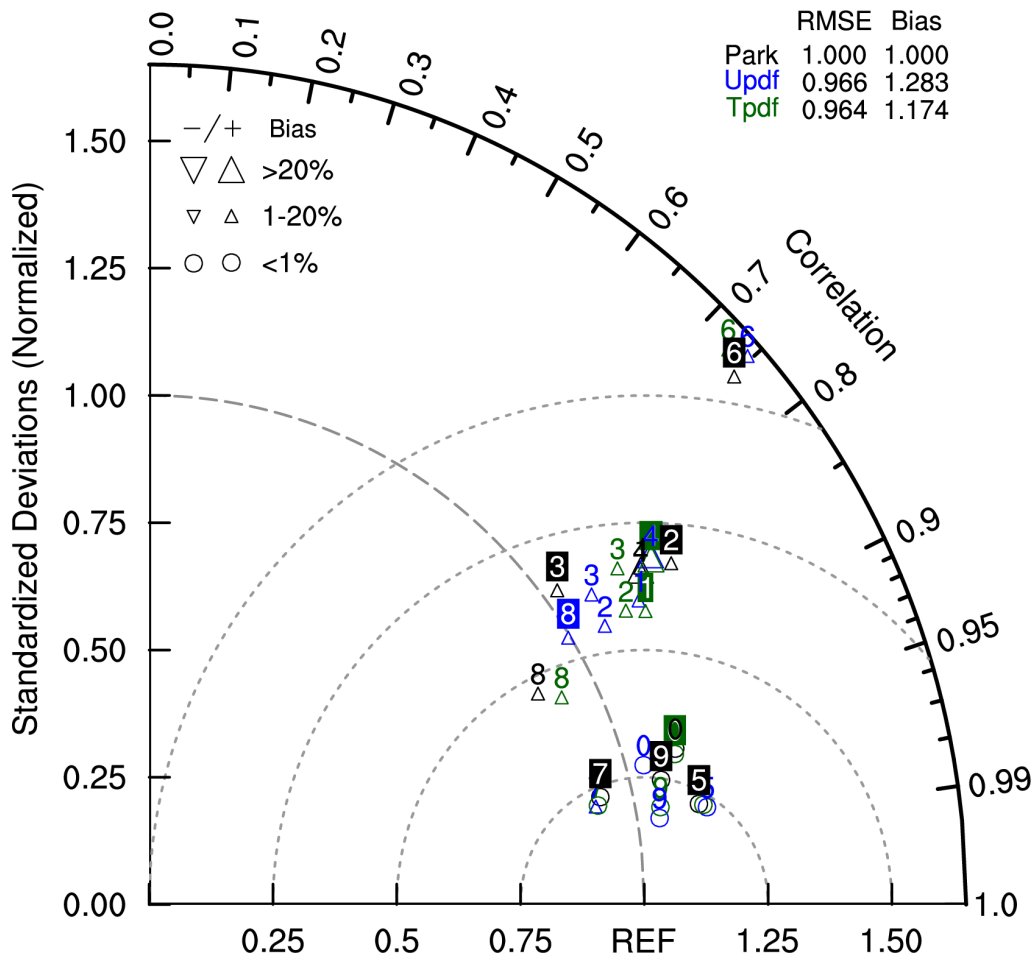


Figure 10. Space-time Taylor diagram for the ten climatic parameters simulated by the three macrophysical schemes (Park: black symbols; U_{pdf}: green; T_{pdf}: blue) and comparisons of these with the corresponding observational data provided by the atmospheric diagnostic package from the NCAR CESM group. The ten climatic parameters are marked from 0 to 9 where 0 denotes sea level pressure; 1 is SW cloud forcing, 2 is LW cloud forcing, 3 is land rainfall, 4 is ocean rainfall, 5 is land 2-m temperature, 6 is Pacific surface stress, 7 is zonal wind at 300 mb, 8 is relative humidity, and 9 is temperature.

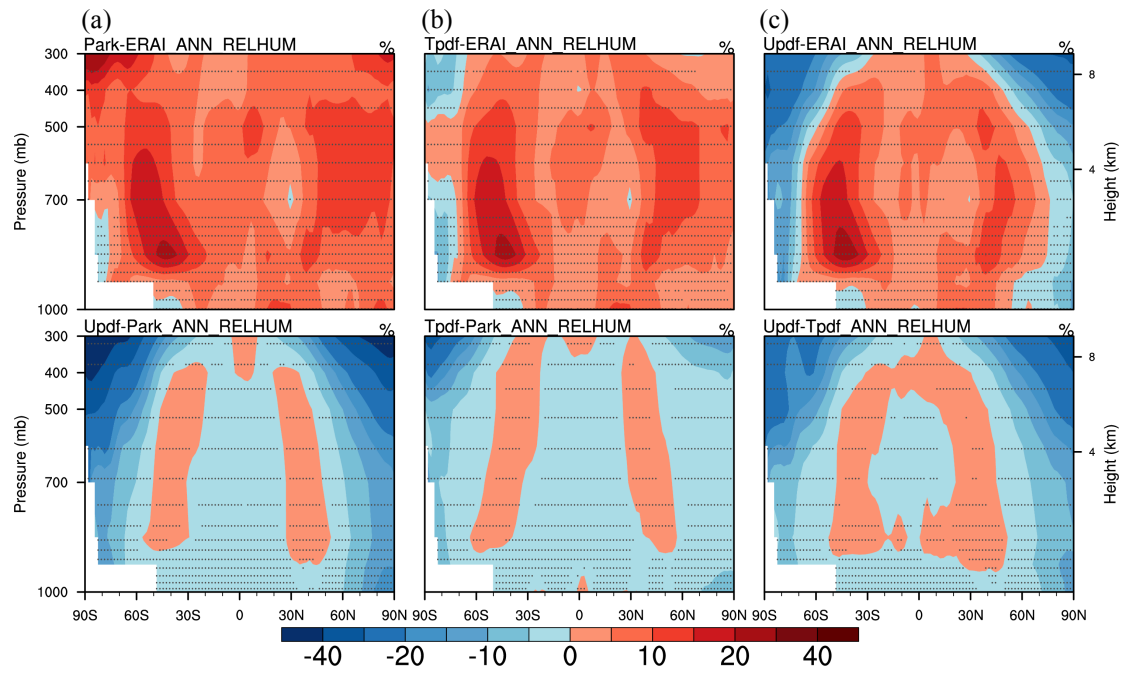


Figure 11. Upper row: latitude–pressure cross-sections of differences in relative humidity (RH) between the simulations and ERA-Interim from (a) Park, (b) T_pdf, and (c) U_pdf schemes. Lower row: differences in RH in pair-wise comparisons of the three cloud macrophysical schemes.

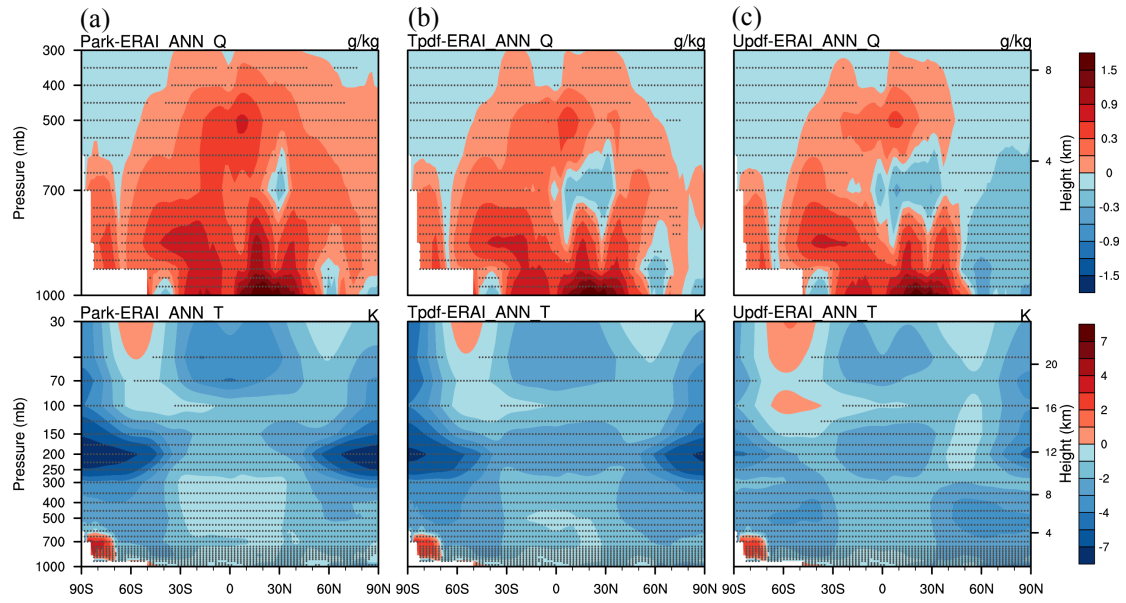


Figure 12. Differences in specific humidity (upper row) and air temperature (lower row) between the simulations and ERA-Interim from the (a) Park, (b) T_pdf, and (c) U_pdf schemes.

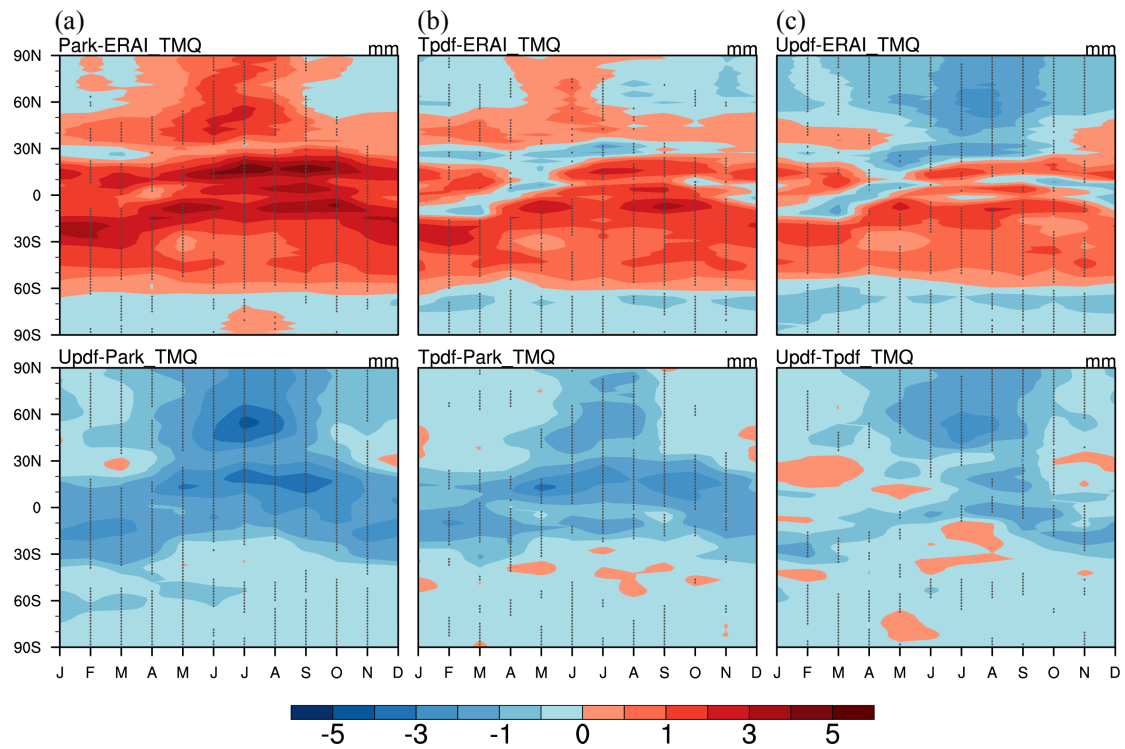


Figure 13. Upper row: differences in annual cycles of zonal mean total precipitable water between the three macrophysical schemes and the ERA-Interim data from the (a) Park, (b) T_pdf, and (c) U_pdf schemes. Lower row: differences in annual cycles of total precipitable water in pair-wise comparisons of the three cloud macrophysical schemes.

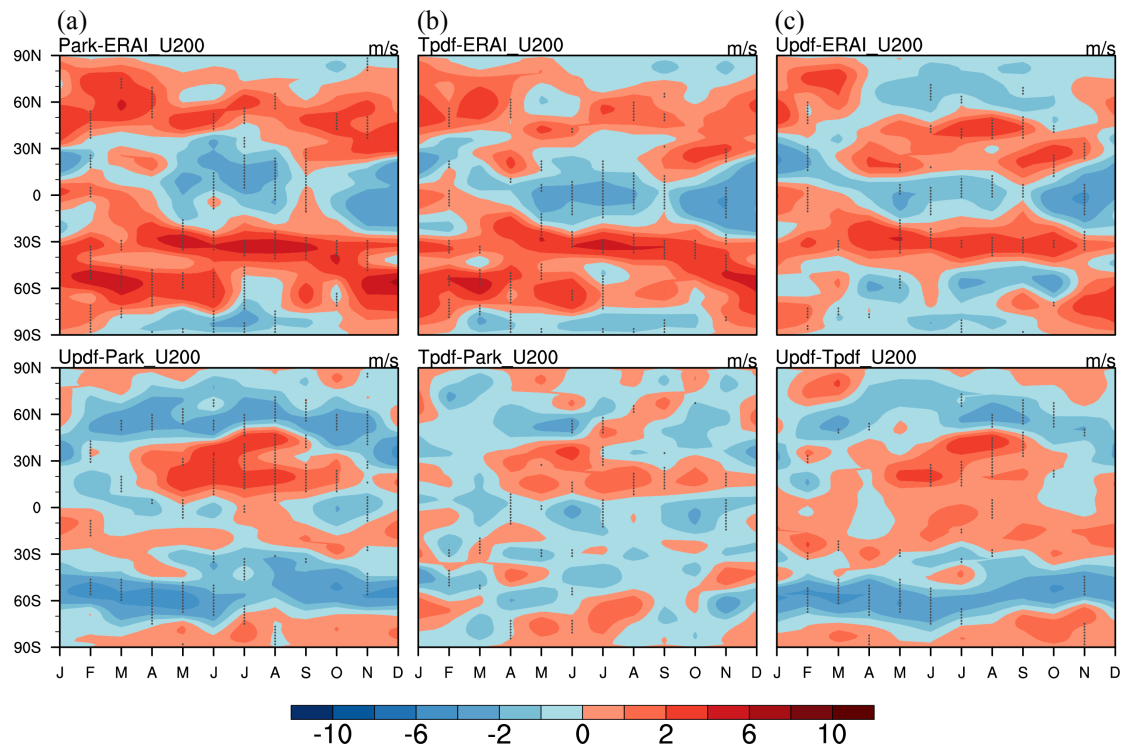


Figure 14. Upper row: differences in annual cycles of zonal wind at 200 mb between the three macrophysical schemes and the ERA-Interim data from the (a) Park, (b) T_pdf, and (c) U_pdf schemes. Lower row: differences in annual cycles of zonal wind at 200 mb in pair-wise comparisons of the three cloud macrophysical schemes.

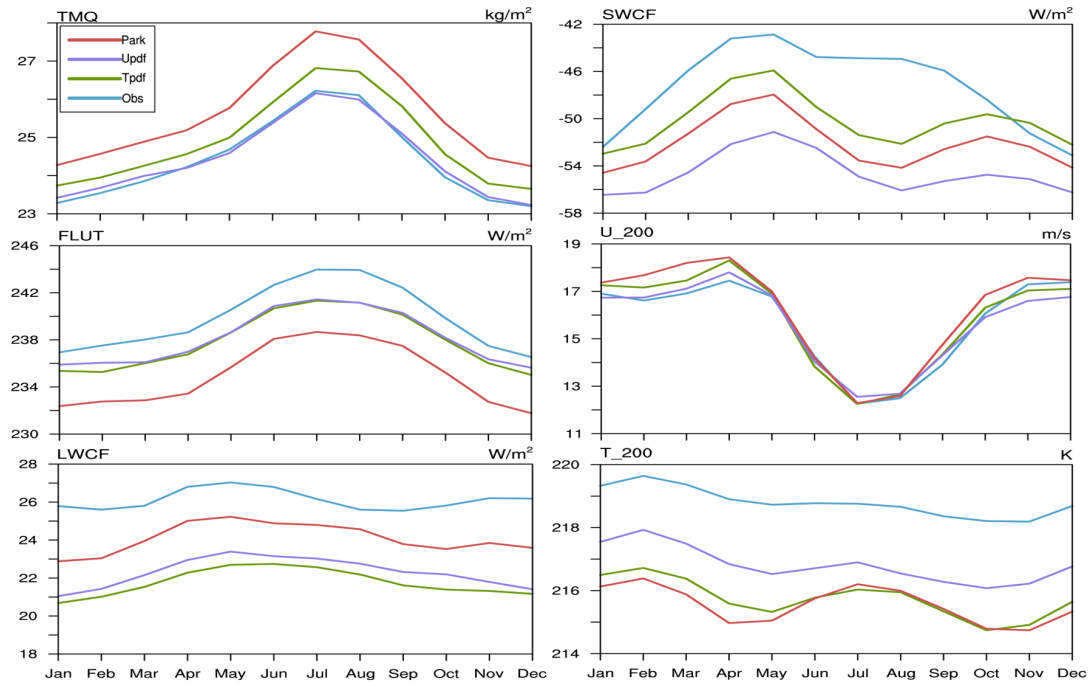


Figure 15. Global annual cycles of (a) total precipitable water, (b) shortwave cloud forcing, (c) net longwave flux at the top of the model, (d) zonal wind at 200 mb, (e) longwave cloud forcing, and (f) air temperature at 200 mb. Colored lines represent observational data (blue) and simulations by the Park (red), U_pdf (purple), and T_pdf (green) schemes.

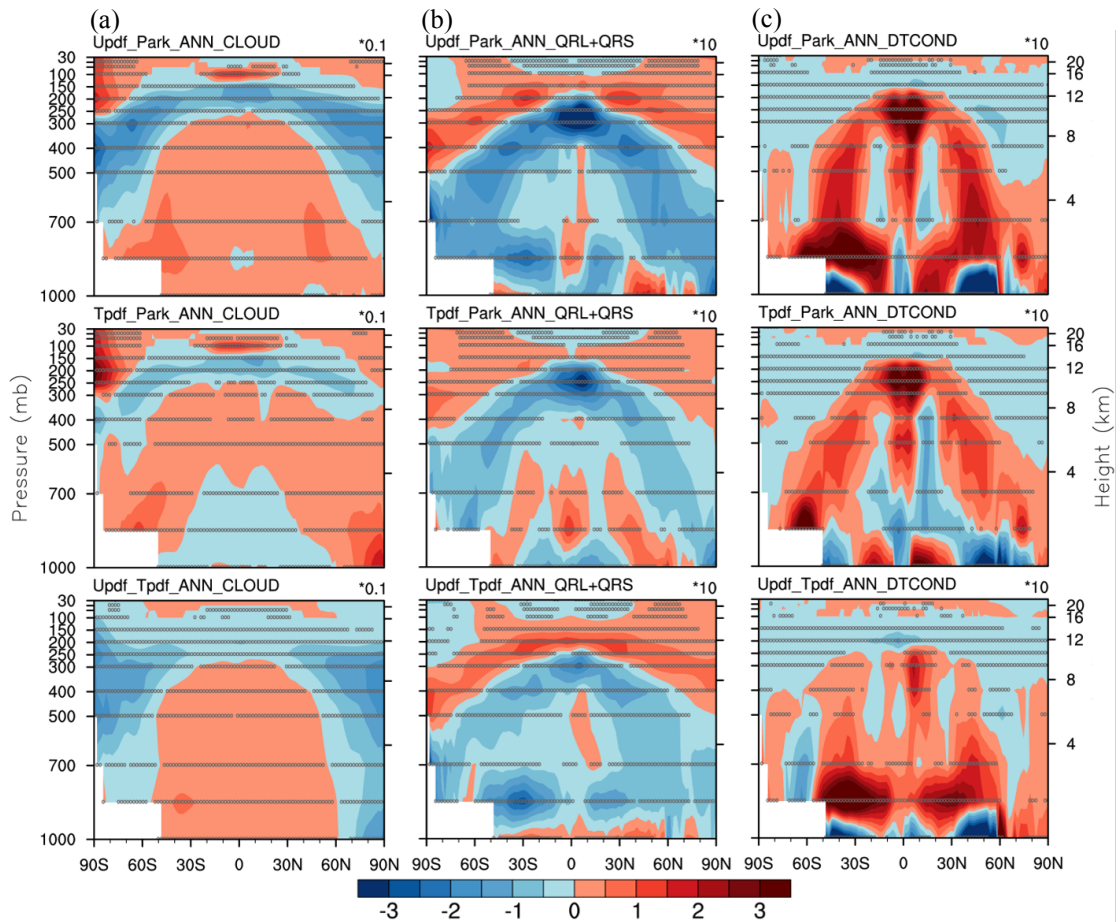


Figure 16. Differences in (a) CF (unit: %), (b) sum of longwave and shortwave heating rates (QRL+QRS, unit: K day^{-1}), and (c) temperature tendencies due to all moist processes in the NCAR CESM model (DTCOND, unit: K day^{-1}) in pair-wise comparisons of the three cloud macrophysical schemes. Upper row: U_pdf and Park; middle row: T_pdf and Park; lower row: U_pdf and T_pdf. A statistically significant difference with a confidence level of 95% is represented in the panels by an open circle using Student's t-test.

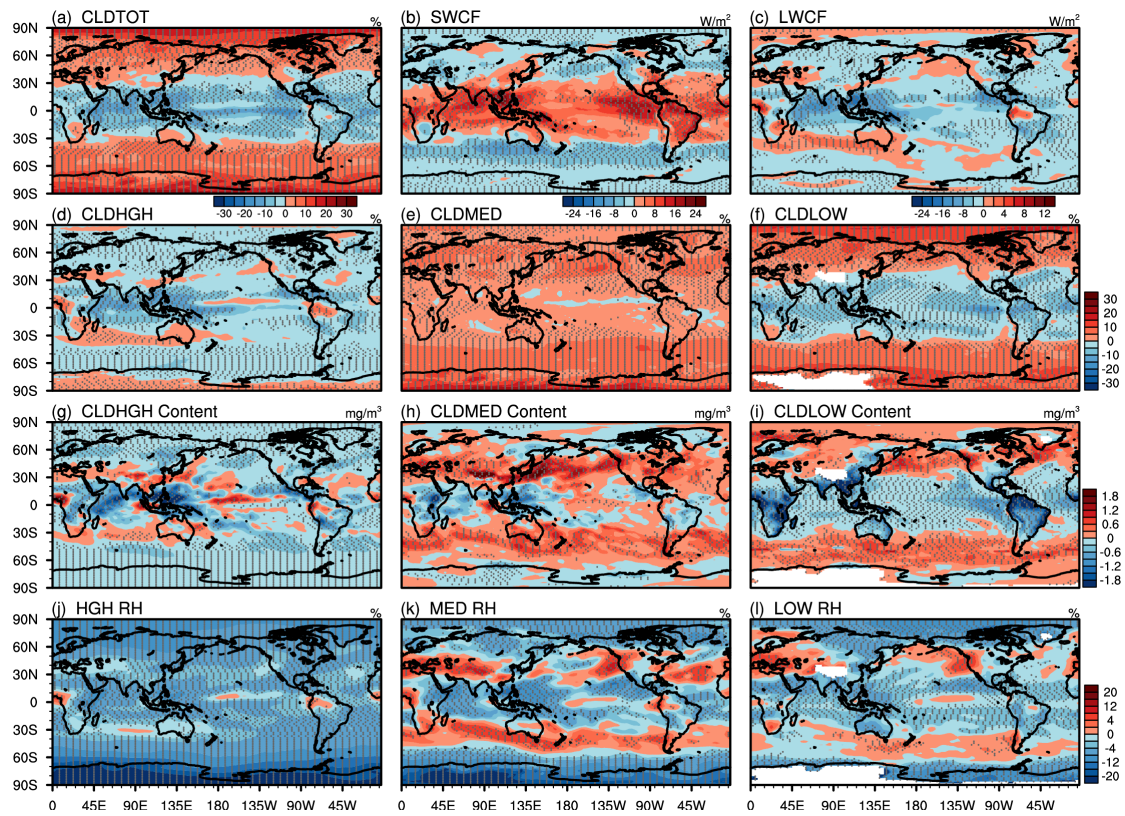


Figure 17. Differences in (a) total cloud fraction, (b) short-wave cloud radiative forcing (W m^{-2}), (c) long-wave cloud radiative forcing (W m^{-2}), and cloud fraction of (d) high clouds, (e) middle clouds, and (f) low clouds between the T_pdf and default Park schemes. (g–i) As for (d–f) but for total cloud water content at the three cloud levels. (j–l) As for (g–i) except for averaged RH at the three cloud levels.